https://doi.org/10.5194/essd-2026-834
Preprint. Discussion started: 4 November 2026
© Author(s) 2026. CC BY 4.0 License.



Open Access Earth System Science Data Discussions

A BPDF database retrieved using multi-angle, multispectral and polarimetric observations from POLDER-3 and DPC-2

Zhe Ji[1,2], Zhengqiang Li[1,2,3*], Gerrit de Leeuw[1,4], Cheng Chen[5], Yahui Che[6], Zihan Zhang[1], Luo Zhang[7]

[1]State Key Laboratory of Remote Sensing and Digital Earth & Key Laboratory of Satellite Remote Sensing of Ministry of Ecology and Environment, Aerospace Information Research Institute, Chinese Academy of Sciences, Beijing 100101, China.
[2]University of Chinese Academy of Sciences, Beijing 100049, China.
[3]State Key Laboratory of Spatial Datum, College of Remote Sensing and Geoinformatics Engineering, Faculty of Geographical Science and Engineering, Henan University, Zhengzhou, 450046, China.
[4]Royal Netherlands Meteorological Institute (KNMI), R&D Satellite Observations, P.O.Box 201, 3730AE De Bilt, The Netherlands.
[5]Anhui Institute of Optics and Fine Mechanics, Hefei Institutes of Physical Science, Chinese Academy of Sciences, Hefei 230031, China.
[6]Institute for Atmospheric Physics, Chinese Academy of Sciences, Beijing 100029, China.
[7]Satellite Application Center for Ecology and Environment, Ministry of Ecology and Environment, Beijing 100094, China.

Corresponding author: Zhengqiang Li (lizq@radi.ac.cn)

Abstract. The bidirectional polarization distribution function (BPDF) characterizes the dependence of land-surface polarized reflectance on illumination and viewing geometry and provides a key surface boundary condition for polarimetric retrievals of aerosol properties. In recent years, the increasing number of polarimeters in orbit has stimulated growing interest in polarized surface reflectance. Reliable multisensor BPDF databases are therefore urgently needed. However, deriving surface polarized reflectance that is comparable across spectral bands and sensors remains challenging. Earlier databases generally corrected only for molecular scattering and adopted the 865 nm results as the final surface polarized reflectance, assuming that aerosol effects were negligible under low aerosol loading and that a single band adequately represented surface polarization. This approach neither explicitly accounted for aerosol effects nor exploited the weak spectral dependence of land-surface polarized reflectance. In fact, even under low-aerosol-loading conditions, across the POLDER-3 and DPC-2 observations used in this study, the relative differences between surface polarized reflectance obtained using molecular-only correction and that obtained by accounting for both molecular and aerosol effects exceeded 10% in approximately 60%–75% of the observations at 490, 670 and 865 nm. Moreover, global BPDF studies have relied primarily on POLDER observations. Because most existing

https://doi.org/10.5194/essd-2026-834
Preprint. Discussion started: 4 November 2026
© Author(s) 2026. CC BY 4.0 License.


studies use observations from 2005–2013, their results may not adequately represent current land-surface conditions. Newly operational polarimeters therefore require an atmospheric-correction method applicable across-sensors to update existing BPDF records and support future BPDF studies. In addition, the effects of mixing among different surface types on BPDF remain poorly understood. Here, we developed a unified atmospheric-correction framework that uses Aerosol Robotic Network (AERONET) aerosol optical depth and vector radiative transfer calculations together with vector radiative-transfer calculations to account for the effects of both atmospheric molecules and aerosols. After correcting the multiband observations, the spectral consistency of the multiband surface polarized reflectance was substantially improved. On this basis, we used weighted fusion to derive a common estimate of surface polarized reflectance from the three corrected bands. The framework was applied to POLDER-3 observations from 2005–2013 and DPC-2 observations from 2022–2023, producing two quality-flagged BPDF databases. The database is publicly available and registered at doi.org/10.57760/sciencedb.015ek. For the cross-sensor evaluation, directional observations acquired under similar surface and observation conditions were matched between the two sensors. The matched directional observations yielded correlation coefficients of 0.60 to 0.87 across 12 International Geosphere–Biosphere Programme (IGBP) land-cover classes, showing clear positive correspondence under similar surface and observation conditions despite the nearly decade-long separation between the two sensor records. The subpixel analysis further showed that the higher-resolution DPC-2 observation sequences were generally more homogeneous, with a mean dominant land-cover fraction 5.8 percentage points higher than that of POLDER-3. After accounting for observation geometry, a lower dominant land-cover fraction was associated with lower surface polarized reflectance, with a greater decrease for POLDER-3 than for DPC-2, indicating a stronger association between surface polarized reflectance and subpixel composition at coarser spatial resolution. The direction of this relationship varied among land-cover classes, showing that subpixel mixing does not produce a uniform monotonic shift but also depends on the polarization contrast between dominant and secondary surface components. By developing a unified atmospheric-correction framework, this study extends BPDF database construction from single-band and single-sensor processing to multiband and multisensor applications. The resulting framework provides a foundation for updating historical BPDF records, developing long-term multisensor records of land-surface polarized reflectance, and improving the surface boundary conditions used in atmospheric polarimetric retrievals.

https://doi.org/10.5194/essd-2026-834
Preprint. Discussion started: 4 November 2026
© Author(s) 2026. CC BY 4.0 License.



1. Introduction

The bidirectional polarization distribution function (BPDF) describes the dependence of surface polarized reflectance on solar and viewing geometry. It is a fundamental representation of the directional anisotropy of polarized surface reflection and also provides the lower boundary condition required for atmospheric radiative transfer calculations. Importantly, the BPDF represents the linearly polarized reflected signal normalized by incident solar irradiance and illumination geometry, rather than the degree of linear polarization itself (Bréon and Maignan, 2017; Maignan et al., 2009). Polarized reflection from land surfaces originates primarily from Fresnel reflection by different surface components. Its magnitude and angular distribution are affected by canopy structure, surface roughness, shadowing, mutual obstruction among surface elements and topographic relief, and therefore vary among land-cover types and observation geometries (Bréon et al., 1995).

Apparent polarized reflectance is jointly affected by scattering and absorption by atmospheric molecules and particles and by surface reflection (Litvinov et al., 2011). Accurate determination of surface polarized reflectance is therefore important not only for understanding the polarimetric properties of land surfaces, but also for improving the accuracy of atmospheric parameter retrievals from polarimetric observations (Hasekamp and Landgraf, 2007; Waquet et al., 2007). Using approximately two months of Polarization and Directionality of the Earth's Reflectances (POLDER) observations, Nadal and Breon (1999) derived empirical BPDFs for 11 surface classes and proposed a semi-empirical model with two parameters. Maignan et al. (2009) subsequently used the longer third generation POLDER record, referred to as POLDER-3, to characterize the directional polarization of natural surfaces and developed a model with a single parameter. Building on these studies, Breon and Maignan (2017) constructed a global BRDF and BPDF dataset from POLDER-3 observations acquired in 2008. The dataset contains representative targets distributed worldwide and organizes the observations according to the 16 land-cover classes of the International Geosphere-Biosphere Programme (IGBP). It has since provided an important observational basis for comparing semi-empirical BPDF models and for training and evaluating data-driven models of surface polarization (He et al., 2020; Liu et al., 2020; Yang et al., 2017).

However, this dataset has several limitations. First, its construction corrected only for molecular scattering and adopted the 865 nm result as the final surface polarized reflectance. This approach assumed that aerosol effects could be neglected under low aerosol loading and that a single band was sufficient to characterize surface polarization (Bréon and Maignan, 2017). It

https://doi.org/10.5194/essd-2026-834
Preprint. Discussion started: 4 November 2026
© Author(s) 2026. CC BY 4.0 License.


neither explicitly accounted for aerosol effects nor exploited the weak spectral dependence of land surface polarized reflectance. However, existing BPDF database construction has not explicitly quantified the residual influence of aerosols under low-aerosol-loading conditions or evaluated whether atmospheric correction improves agreement among the three polarized bands. Reliance on a single band also prevents the comparatively weak spectral dependence of land-surface polarized reflectance from being used as an internal constraint on the corrected surface signal. Second, when Breon and Maignan (2017) constructed this dataset, few other spaceborne polarimetric observations were available for global land surface BPDF studies. Global BPDF research therefore relied primarily on POLDER observations. However, POLDER observations are limited to the period from 2005 to 2013 and were acquired many years ago. Because land cover and surface conditions can change over time, these historical observations may no longer adequately represent current surface conditions. As the number of new polarimeters in orbit increases, the demand for reliable BPDF databases continues to grow, while existing BPDF databases are increasingly unable to meet current research needs. The development of reliable multisensor BPDF databases is therefore both necessary and urgent.

The second generation Directional Polarization Camera (DPC-2) provides an opportunity to extend the observational record beyond the POLDER-3 era and to develop an atmospheric correction framework applicable across-sensors (Ji et al., 2025; Zhang et al., 2025). DPC-2 has the same polarized bands and a similar observation configuration to POLDER-3. It also has a finer spatial resolution and provides more viewing directions than POLDER-3. The difference in spatial resolution between the two sensors further enables the effects of spatial sampling and subpixel land-cover heterogeneity on the BPDF to be examined.

Using DPC-2 observations together with ground based aerosol observations from the Sun-sky Radiometer Observation Network (SONET), Liu et al. (2026) constructed the regional BPDF-DPC-CN dataset for China and compared six semi-empirical BPDF models. However, this study did not resolve several key issues in BPDF research. First, its results are limited to China. Second, an empirical formula was used to correct aerosol effects in only the 865 nm band, and the uncertainty associated with the empirical aerosol correction under low aerosol loading was not quantified. Finally, the applicability of the atmospheric correction scheme to different polarimeters was not evaluated. Although this study improved existing approaches to BPDF database construction, it did not achieve the goal of establishing a reliable multisensor BPDF database.

https://doi.org/10.5194/essd-2026-834
Preprint. Discussion started: 4 November 2026
© Author(s) 2026. CC BY 4.0 License.


To address these limitations, this study has three objectives. First, we develop an atmospheric correction framework that uses aerosol optical depth from the globally distributed Aerosol Robotic Network (AERONET) together with radiative transfer calculations from the Second Simulation of a Satellite Signal in the Solar Spectrum vector model (6SV) (Kotchenova et al., 2006). Surface polarized reflectance is retrieved separately at 490, 670 and 865 nm, and the band-specific results are combined through weighted multiband fusion by exploiting the comparatively weak spectral dependence of land-surface polarized reflectance. Second, we apply the same atmospheric correction, data organization and quality-assurance framework to POLDER-3 observations from 2005 to 2013 and DPC-2 observations from 2022 to 2023. We then evaluate the sampling characteristics, angular distributions, conditional cross-sensor consistency and semi-empirical BPDF model fitting of the two databases. Third, we quantify subpixel land-cover heterogeneity from the fractional IGBP composition of each satellite pixel and examine its association with surface polarized reflectance at the two sensor resolutions.

To our knowledge, this study is the first to use a unified atmospheric correction procedure, data organization scheme and quality control framework to construct two BPDF databases from observations distributed across global land regions from POLDER-3 and DPC-2 observations, while retaining the original angular sampling and spatial resolution characteristics of the respective sensors. This study thereby extends BPDF database construction from single band and single sensor processing to a multiband and multisensor framework. It provides a foundation for updating historical BPDF records, constructing long-term multisensor records of land surface polarized reflectance and improving the surface boundary conditions required for atmospheric polarimetric remote sensing retrievals.

2. Materials

2.1. POLDER-3 data

POLDER-3, carried onboard the Polarization and Anisotropy of Reflectances for Atmospheric Science coupled with Observations from a Lidar (PARASOL) satellite, acquired multi-angle measurements in nine visible and near-infrared spectral channels between 443 and 1020 nm. Polarization was measured at 490, 670, and 865 nm, and the instrument could observe the same target from up to 12 directions (Tanré et al., 2011). The POLDER-3 data used in this study have a spatial resolution of

https://doi.org/10.5194/essd-2026-834
Preprint. Discussion started: 4 November 2026
© Author(s) 2026. CC BY 4.0 License.


125 approximately 6.1 km. The POLDER-3 record used here covers March 2005 to October 2013. Its three polarization channels coincide with those of DPC-2, allowing the two records to be processed using the same spectral definition of polarized reflectance.

2.2. DPC-2 data

DPC-2, carried aboard the GF-5(02) satellite, is a wide-field, multi-angle imaging polarimeter that measures reflected radiation
130 in eight spectral channels between 443 and 910 nm. A ground target can be observed from up to 17 viewing directions during a single overpass (Ji et al., 2025; Zhang et al., 2025). The DPC-2 data used in this study has a nominal spatial resolution of approximately 3.3 km, and the observations cover the period from March 2022 to August 2023. The polarized measurements at 490, 670 and 865 nm were selected because these channels are common to POLDER-3 and DPC-2. For each viewing direction, the corresponding solar zenith angle (SZA), viewing zenith angle (VZA), and relative azimuth angle (RAA) were
135 retained. Total radiances at 670 and 865 nm were also used to calculate the normalized difference vegetation index (NDVI). POLDER-3 and DPC-2 therefore provide comparable spectral and geometric information but differ in acquisition period, directional sampling, and spatial resolution.

2.3. AERONET data

AERONET is a global network of standardized Sun–sky photometers (Holben et al., 1998). We used AERONET Version 3
140 Level 1.5 spectral AOD products, which are cloud screened and subject to automated quality controls. AERONET AOD typically has an uncertainty of approximately 0.01 at visible and near-infrared wavelengths (Giles et al., 2019). AERONET was used to characterize the aerosol conditions required for atmospheric correction rather than as an independent validation data set. To this end, satellite observations within 50 km of an AERONET site were used. AERONET AOD was used both as an input to the 6SV atmospheric correction and to exclude observations that did not satisfy the prescribed low-aerosol-loading
145 criterion.

https://doi.org/10.5194/essd-2026-834
Preprint. Discussion started: 4 November 2026
© Author(s) 2026. CC BY 4.0 License.



2.4. MCD12Q1 product

Land-cover information was obtained from the Moderate Resolution Imaging Spectroradiometer (MODIS) Terra and Aqua combined MCD12Q1 Collection 6.1 product, which provides annual global land-cover maps at a nominal spatial resolution of 500 m. We used the LC_Type1 layer, which follows the International Geosphere-Biosphere Programme (IGBP) classification scheme (Sulla-Menashe et al., 2019). For each POLDER-3 and DPC-2 pixel, the area fraction of every IGBP class was calculated over the valid classified area. The class occupying the largest fraction of the pixel was defined as the dominant land-cover class, and its fractional coverage was retained to characterize surface homogeneity and derive the mixing index used in the subsequent analysis. Each satellite observation was matched to the MCD12Q1 land-cover product for the corresponding acquisition year.

3. Methods

3.1. Basic principles

The apparent polarized reflectance (ρ_{p}) at the top of the atmosphere (TOA) was calculated from the linear-polarization components of the Stokes vector as:

$$\rho_{\mathrm{p}} = \frac{\pi\sqrt{Q^2 + U^2}}{E_0 \cos(\theta_{\mathrm{s}})} \tag{1}$$

where Q and U are the linear polarization components of the Stokes vector, E_0 is the solar irradiance at the TOA, θ_{s} is the SZA.

Following Waquet et al. (2009), the TOA apparent polarized reflectance was represented as the sum of the polarized atmospheric path reflectance and the surface contribution transmitted through the atmosphere.

$$\rho_{\mathrm{p}} = \rho_{\mathrm{p0}} + T^{\downarrow}(\theta_{\mathrm{s}}) R_{\mathrm{p}} T^{\uparrow}(\theta_{\mathrm{v}}) \tag{2}$$

where ρ_{p0} denotes the polarized path reflectance, R_{p} is the surface polarized reflectance. $T^{\downarrow}$ and $T^{\uparrow}$ describe the downward and upward transmission, respectively.

https://doi.org/10.5194/essd-2026-834
Preprint. Discussion started: 4 November 2026
© Author(s) 2026. CC BY 4.0 License.

Open Access Earth System Science Data Discussions

3.2. Atmospheric correction

We used the 6SV vector radiative transfer model to atmospherically correct apparent polarized reflectance and retrieve surface polarized reflectance. For each spectral band and observation geometry, 6SV was used to calculate the polarized path reflectance and the downward and upward atmospheric transmittances. Surface polarized reflectance was then retrieved by solving Eq. (2). To constrain the aerosol conditions required for atmospheric correction, we used AERONET observations acquired within ±30 min of the satellite overpass and matched them to satellite pixels located within a radius of 50 km around each AERONET site. This spatiotemporal matching assumes that aerosol conditions vary slowly over the corresponding temporal and spatial scales. As aerosol loading increases, the surface contribution becomes progressively more difficult to separate from the atmospheric polarization signal. We therefore retained only observations with $AOD_{550} < 0.1$. Although this threshold inevitably reduces the number of available observations, particularly in regions where aerosol loading remains high for extended periods, it helps reduce uncertainty in the atmospheric correction and thereby enables more reliable retrievals of surface polarized reflectance.

AERONET direct-sun measurements provide well constrained estimates of AOD. However, AOD alone is insufficient for the 6SV calculations because the model also requires additional aerosol optical and microphysical parameters. These parameters are commonly retrieved from AERONET sky radiance measurements, but their uncertainties increase as aerosol loading decreases (Giles et al., 2019). In particular, the quality assurance criteria for several key retrieved aerosol parameters require AOD_{440} to be at least 0.4 (Sinyuk et al., 2020). Because this study retained only observations with AOD_{550} below 0.1, the corresponding sky radiance retrievals generally did not meet these quality requirements and could not provide reliable and complete aerosol model inputs for individual observations. A prescribed prescribed continental aerosol model was therefore required. Because reliable observation-specific aerosol microphysical inputs were unavailable under these low-AOD conditions, the 6SV prescribed continental aerosol model was adopted as a common baseline for the global land observations. To assess the influence of this prescribed prescribed continental aerosol model on the atmospheric correction, we compared the polarized atmospheric path reflectance simulated using the six aerosol models defined by Omar et al. (2005) at a fixed AOD_{550} of 0.1 across different wavelengths and observation geometries in Supplementary Section S1. Identical observation geometries were used for all six models at 490, 670 and 865 nm, thereby isolating differences attributable to aerosol model

https://doi.org/10.5194/essd-2026-834
Preprint. Discussion started: 4 November 2026
© Author(s) 2026. CC BY 4.0 License.


selection from those caused by variations in aerosol loading or angular sampling. The differences among the six models were small over most of the sampled angular domain, but could not be neglected at large solar zenith angles and under oblique viewing conditions.

3.3. Multiband fusion and spectral consistency assessment

Previous studies have shown that surface polarized reflectance has comparatively weak spectral dependence across the visible and near-infrared wavelengths (Waquet et al., 2009). However, band-specific retrievals remain affected by residual atmospheric correction errors, instrument response, measurement errors, and spectral differences among surface components. The retrieved R_p can therefore differ among the three bands. As shown in Section 4.2, before fusion, the cross-band dispersion of surface polarized reflectance retrieved after correcting for both molecular and aerosol effects was markedly lower than that of apparent polarized reflectance before atmospheric correction. This indicates that the spectral differences after atmospheric correction were closer to theoretical expectations. On this basis, we applied multiband weighted least-squares fusion to reduce the influence of deviations in any single band and derive an R_p that represents the surface polarization signal shared across the bands. For each viewing direction, the band-specific R_p were first screened using the validity criteria described in Supplementary Section S2. The final estimate was then determined by minimizing the sum of the weighted squared deviations between the fused estimate and the valid band-specific values. Because the atmospheric polarized contribution is generally stronger at shorter wavelengths, the results at 490 and 670 nm are more susceptible to residual atmospheric correction errors. Greater weights were therefore assigned to the longer wavelengths. To prevent a single anomalous band from exerting a disproportionate influence on the fused result. When all three bands were valid, a robust outlier test was applied to identify a single strongly discrepant band. If the criterion was met, that band was excluded and the remaining valid bands were used for fusion. The validity criteria, minimum number of bands, default weights, outlier criterion, weight renormalization, and treatment of missing values are described in Supplementary Section S2. The fused result represents the surface polarization signal jointly constrained by the valid bands and does not correspond to any individual wavelength. Genuine spectral differences are reflected in the residuals between the band-specific and fused results but are not retained in the final fused result.

https://doi.org/10.5194/essd-2026-834
Preprint. Discussion started: 4 November 2026
© Author(s) 2026. CC BY 4.0 License.

Open Access Earth System Science Data Discussions

3.4. Characterization of database sampling

The purpose of this analysis was to identify differences in the observation targets and geometries represented in the two databases, thereby establishing the sampling basis for subsequent comparisons between the sensors. An observation sequence was defined as the set of valid directional measurements acquired for one satellite pixel during a single satellite overpass. Each valid viewing direction within that sequence was defined as a directional observation. The term pixel is used to describe the spatial footprint and its subpixel land-cover composition. When characterizing the land-cover distributions of the two databases, each observation sequence was counted only once. This prevented sequences containing more valid viewing directions from receiving greater weight. Spatial sampling density was defined as the number of observation sequences within each cell of a regularly spaced geographical grid. Because POLDER-3 and DPC-2 cover different observation periods, the number of observation sequences in each grid cell was normalized separately within each database. The normalized spatial sampling densities describe the relative distribution of observations within each database rather than absolute differences in observation frequency between the two sensors. Land-cover composition was represented by the proportion of observation sequences associated with each dominant IGBP class. This comparison was used to determine whether the same land-cover classes were represented in different proportions in the two databases. To reduce the influence of uneven sampling among observation geometries on the R_p statistics, R_p was first binned onto a common angular grid within each original IGBP class. When broader surface groups were subsequently constructed, the directional R_p distributions of the constituent IGBP classes were averaged using equal class weights. Each IGBP class therefore contributed equally to the directional characteristics of its broader surface group, irrespective of its sample size.

3.5. BPDF quality assurance

The same quality-assurance framework was applied to the POLDER-3 and DPC-2 BPDF databases to characterize the internal quality of the multi-angle R_p observations. Each directional observation was assigned a QA flag containing one of four grades, from QA_0 to QA_3, with QA3 denoting the highest internal quality. The framework separately evaluates QA components that describe the complete observation sequence and those associated with an individual directional observation.. At the observation-sequence level, the evaluated factors include aerosol loading, surface homogeneity, and the number and angular

https://doi.org/10.5194/essd-2026-834
Preprint. Discussion started: 4 November 2026
© Author(s) 2026. CC BY 4.0 License.



coverage of valid viewing directions. As aerosol loading increases, the polarized atmospheric contribution becomes stronger. When a prescribed prescribed continental aerosol model is used, the surface signal consequently becomes more difficult to separate from the atmospheric contribution. Aerosol loading was therefore included in the quality assessment (Vermote et al., 1997). Surface homogeneity was also evaluated because R_{p} becomes less representative of the dominant land-cover class as the contributions from other land-cover classes increase. An insufficient number of valid viewing directions or limited angular coverage reduces the ability of an observation sequence to represent the surface BPDF. At the individual directional observation level, SZA and VZA were evaluated separately. Oblique illumination and viewing geometries increase the atmospheric path length and may amplify residual atmospheric correction errors (Franch et al., 2013). Highly oblique geometries also depart more strongly from the plane-parallel assumptions adopted in the radiative transfer calculations (Dahlback and Stamnes, 1991). The directional-observation level assessment was then combined with the observation-sequence level assessment and the validity of each atmospherically corrected spectral band. Because the final R_{p} was obtained through spectral fusion, the quality values of the participating bands were propagated using the same band participation mask and spectral weights used in the R_{p} fusion. Detailed definitions and calculations are provided in Supplementary Section S4.

3.6. Cross-sensor consistency assessment

The fused R_{p} from POLDER-3 and DPC-2 were compared by matching directional observations acquired under similar conditions. Their R_{p} were therefore compared by matching directional observations acquired under similar conditions. For each directional observation, the dominant IGBP class, spatial location, and NDVI were determined by the observation sequence to which it belonged, whereas the solar and viewing geometry described the specific directional observation. Candidate directional observations were required to represent the same dominant IGBP class and to have similar spatial locations, solar and viewing geometries, and NDVI. These constraints reduce differences caused by surface type, spatial mismatch, directional reflectance, and vegetation state during comparisons between sensors (Franks et al., 2017; Jethva et al., 2014; Lallart et al., 2008). A reciprocal nearest neighbour procedure was used to prevent the same directional observation from being included in multiple matched pairs. For each POLDER-3 directional observation, the nearest eligible DPC-2 directional observation was identified, and the same procedure was applied in the opposite direction. A pair was retained only when the

https://doi.org/10.5194/essd-2026-834
Preprint. Discussion started: 4 November 2026
© Author(s) 2026. CC BY 4.0 License.

Open Access Earth System Science Data Discussions

two directional observations were the nearest eligible candidates for each other. Each directional observation therefore contributed to no more than one matched pair between the sensors. This procedure allowed R_p from the POLDER-3 and DPC-2 databases to be compared under similar surface types, spatial locations, observation geometries, and vegetation states. The comparison therefore assesses the conditional consistency of the fused R_p between the two sensor records under similar surface and observation conditions. Detailed matching criteria and calculations are provided in Supplementary Section S5.

3.7. Cross-database comparison of semi-empirical BPDF model fitting

The angular structure of the two databases was compared with six established semi-empirical BPDF formulations: Nadal–Bréon, Waquet, Diner, Maignan, Litvinov, and Xie–Cheng (Diner et al., 2012; Litvinov et al., 2011; Maignan et al., 2009; Nadal and Breon, 1999; Waquet et al., 2009; Xie et al., 2017). Each model was fitted independently to the multi-angle R_p sequence of each pixel. The comparison was restricted to observations with all nominal viewing positions, so that differences in model performance were not driven by missing angular observations. All models were fitted using a common nonlinear least-squares protocol. Fitting agreement was summarized separately by viewing position and dominant IGBP class. The model equations and detailed procedure are described in Supplementary Section S6.

3.8. Mixing index and sampling uncertainty

We used the mixing index (MI) to characterize subpixel land-cover mixing. For each pixel, MI was defined as MI = 1 - f_{dom}, where f_{dom} is the fractional area of the dominant MCD12Q1 IGBP class within the valid classified portion of the satellite pixel. An MI of 0 indicates that no contribution from nondominant land-cover classes was detected, whereas larger MI values indicate a greater combined contribution from these classes. An increase of 0.1 in MI is equivalent to a 10 percentage point decrease in the fractional area of the dominant land-cover class. We first compared the MI distributions of the two sensors using all valid observation sequences and calculated the mean MI within each dominant IGBP class. These comparisons determine whether the two spatial resolutions represent different levels of subpixel land-cover heterogeneity. The relationship between MI and R_p was then evaluated using two complementary approaches. For the descriptive analysis, each pixel was represented by the median R_p of all its valid directional observations. Pixel-level median R_p was then compared across MI intervals. This

https://doi.org/10.5194/essd-2026-834
Preprint. Discussion started: 4 November 2026
© Author(s) 2026. CC BY 4.0 License.



approach prevents pixels containing more valid viewing directions from exerting a disproportionate influence on the descriptive statistics. Regression analyses were used to estimate the association between MI and R_p for each sensor as a whole and within each IGBP class. The models included linear and quadratic terms for standardized SZA, VZA, and RAA. Because the response of R_p to solar and viewing geometry is generally nonlinear, including both terms approximates the main nonlinear geometric variation and reduces interference from differences in observation geometry when estimating the association between MI and R_p. Each directional observation was weighted by the reciprocal of the number of valid directions contributed by its source pixel. The weights of all directional observations from a given pixel therefore sum to approximately one, giving pixels with different numbers of valid directions approximately equal total weight. After adjustment for the geometry terms included in the model, the reported MI coefficient represents the adjusted mean change in R_p associated with a 0.1-unit increase in MI. Because observations acquired on the same date, within the same geographical region, or from the same pixel may be correlated, sampling uncertainty was quantified using two-way cluster-robust covariance estimation, with acquisition date and equal-area spatial cells as the two clustering dimensions. This approach allows observations to be correlated within either dimension without requiring a predefined parametric correlation structure. The sensor-wide regression models additionally included dominant IGBP class as a fixed effect. Class-specific P values were adjusted using the Benjamini and Hochberg, (1995) procedure to control the false-discovery rate within each sensor, and the adjusted values are reported as q values. The two-way cluster-robust covariance estimation followed Cameron et al. (2011) and Cameron and Miller (2015). Sample definitions, descriptive binning, regression specifications, cluster construction, confidence interval calculations and multiple-testing procedures are provided in Supplementary Section S6.

3.9. BPDF database specification

The POLDER-3 and DPC-2 BPDF databases are provided in comma-separated value (CSV) format. Each row represents one multi-angle observation sequence for a satellite pixel on a given acquisition date. The sequence-level fields contain the acquisition date, pixel-centre coordinates, surface elevation, and dominant IGBP class. The direction-specific fields contain the SZA, VZA, RAA, atmospherically corrected surface polarized reflectance at 490, 670, and 865 nm, the spectrally fused surface polarized reflectance, and its overall quality-assurance grade. A DPC-2 observation sequence contains up to 17 viewing

https://doi.org/10.5194/essd-2026-834
Preprint. Discussion started: 4 November 2026
© Author(s) 2026. CC BY 4.0 License.



directions, while a POLDER-3 observation sequence contains up to 12. The product fields are listed in Table 1, and the detailed file structure is described in Supplementary Section S7.

Table 1 Fields included in the POLDER-3 and DPC-2 BPDF databases.

Field	Data level	Description
Year, Month, Day	Observation sequence	Acquisition date
Lat, Lon	Observation sequence	Latitude and longitude of the pixel centre in degrees
HEIGHT	Observation sequence	Surface elevation in kilometres
IGBP	Observation sequence	Dominant IGBP land-cover class
SZA_i	Directional observation	Solar zenith angle in degrees
VZA_i	Directional observation	Viewing zenith angle in degrees
RAA_i	Directional observation	Relative azimuth angle in degrees
Rp_490_i	Directional observation	Atmospherically corrected surface polarized reflectance at 490 nm
Rp_670_i	Directional observation	Atmospherically corrected surface polarized reflectance at 670 nm
Rp_865_i	Directional observation	Atmospherically corrected surface polarized reflectance at 865 nm
Rp_i	Directional observation	Surface polarized reflectance obtained by multiband fusion
qa_overall_i	Directional observation	Overall quality-assurance grade, ranging from QA_0 to QA_3

Here, i denotes the viewing-direction index. It ranges from 0 to 16 for DPC-2 and from 0 to 11 for POLDER-3. The polarized-reflectance variables are dimensionless.

4. Atmospheric-correction sensitivity and internal spectral consistency

4.1. Necessity of accounting for aerosol effects in atmospheric correction

Using the 6SV atmospheric correction framework described above, we applied two correction schemes to the same satellite observations to evaluate the sensitivity of R_{p} to aerosol treatment. In the first scheme, AOD was set to zero and only molecular effects were considered. The resulting surface polarized reflectance is denoted $R_{\mathrm{p}}^{\mathrm{mol}}$. In the second scheme, the AERONET

https://doi.org/10.5194/essd-2026-834
Preprint. Discussion started: 4 November 2026
© Author(s) 2026. CC BY 4.0 License.



Open Access Earth System Science Data Discussions

AOD and the prescribed prescribed continental aerosol model were used to account for both molecular and aerosol effects. The resulting surface polarized reflectance is denoted $R_{\mathrm{p}}^{\mathrm{mol+aer}}$. The difference between the two schemes was defined as $\Delta R_{\mathrm{p}} = R_{\mathrm{p}}^{\mathrm{mol}} - R_{\mathrm{p}}^{\mathrm{mol+aer}}$.

All analyses below use observations with $\mathrm{AOD}_{550} < 0.1$, consistent with the criterion used to construct the databases. Within this range, the absolute difference $|\Delta R_{\mathrm{p}}|$ increases with AOD_{550} (Figure 1a) and shows a pronounced dependence on scattering angle. The difference remains relatively large between approximately 45° and 110° and decreases rapidly beyond 120° (Figure 1b). Although aerosol scattering is generally weaker at 865 nm than at 490 and 670 nm, the difference between the two correction schemes is larger at 865 nm. This does not indicate stronger aerosol scattering at 865 nm because ΔR_{p} represents the net effect of aerosol induced changes in polarized path reflectance and atmospheric transmittance rather than the aerosol path contribution alone. The observed wavelength differences describe the spectral sensitivity of atmospheric correction to aerosol treatment rather than the intrinsic spectral dependence of R_{p}. They therefore do not conflict with the multiband fusion based on the weak spectral dependence of surface polarized reflectance. Overall, neglecting aerosol effects introduces differences in R_{p} that vary with wavelength and observation geometry rather than a fixed offset.

To evaluate the magnitude of these differences relative to the surface polarized signal, the aerosol relative difference F_{aer} was defined as $F_{\mathrm{aer}} = \left[\left(R_{\mathrm{p}}^{\mathrm{mol}} - R_{\mathrm{p}}^{\mathrm{mol+aer}}\right)/R_{\mathrm{p}}^{\mathrm{mol}}\right] \times 100\%$. Here, $|\Delta R_{\mathrm{p}}|$ describes the absolute difference between the two correction schemes, whereas F_{aer} expresses this difference relative to $R_{\mathrm{p}}^{\mathrm{mol}}$ and therefore characterizes the sensitivity of the retrieved R_{p} to aerosol treatment. The median F_{aer} within the AOD_{550} bins is generally a few percent at 490 nm and approximately 10% to 20% at 670 and 865 nm (Figure 1c). The median F_{aer} is generally positive, indicating that $R_{\mathrm{p}}^{\mathrm{mol}}$ is typically higher than $R_{\mathrm{p}}^{\mathrm{mol+aer}}$. When aerosols are included, part of the apparent polarized signal is attributed to the aerosol related atmospheric contribution and atmospheric transmittance is recalculated. The retrieved surface R_{p} is therefore lower for most observations. The exceedance fraction was defined as the proportion of valid observations for which $|F_{\mathrm{aer}}|$ exceeds a specified threshold. Among observations with $\mathrm{AOD}_{550} < 0.1$, approximately 60% at 490 nm and approximately 75% at both 670 and 865 nm have $|F_{\mathrm{aer}}| > 10\%$ (Figure 1d). Large relative differences therefore occur across a substantial fraction of the low aerosol loading sample rather than being driven by a small number of extreme observations. These results show that aerosol effects must be explicitly considered in atmospheric correction even when $\mathrm{AOD}_{550} < 0.1$.

https://doi.org/10.5194/essd-2026-834
Preprint. Discussion started: 4 November 2026
© Author(s) 2026. CC BY 4.0 License.

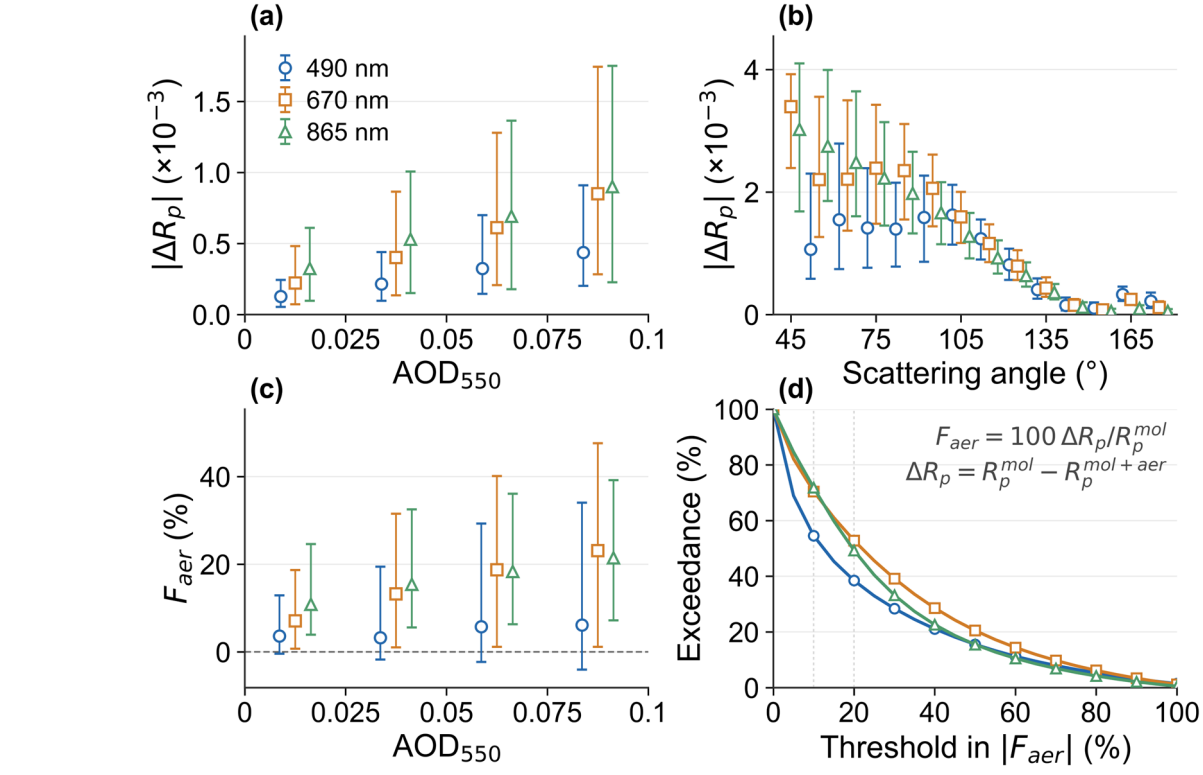


Figure 1. Sensitivity of retrieved land-surface polarized reflectance to aerosol treatment. (a) Absolute difference $|\Delta R_p|$) as a function of AOD$_{550}$. (b) $|\Delta R_p|$ as a function of scattering angle. (c) Aerosol relative difference F_{aer} as a function of AOD$_{550}$. (d) Fractions of valid observations for which $|F_{aer}|$ exceeds the specified thresholds at 490, 670 and 865 nm. All panels include only observations with AOD$_{550}$ below 0.1.

4.2. Spectral consistency of land-surface polarized reflectance

To evaluate whether atmospheric correction improved the internal cross-band consistency of land-surface polarized reflectance, we performed pairwise comparisons among the 490, 670 and 865 nm bands separately for POLDER-3 and DPC-2. The three band pairs comprised 490 and 670 nm, 490 and 865 nm, and 670 and 865 nm (Figure 2). Each comparison included only the same directional observations for which both bands were valid. Before atmospheric correction, the comparisons were based on apparent polarized reflectance at the top of the atmosphere. After atmospheric correction, they were based on band-specific R_p retrieved by accounting for both molecular and aerosol effects. For each band pair, consistency was evaluated using the correlation coefficient, root mean square error and bias. The root mean square error represents the overall difference between the two bands for the same directional observations. Bias was calculated as the value at the shorter wavelength minus that at

https://doi.org/10.5194/essd-2026-834
Preprint. Discussion started: 4 November 2026
© Author(s) 2026. CC BY 4.0 License.



the longer wavelength and therefore represents the systematic offset between the two bands. The percentage reduction in root mean square error was calculated relative to the corresponding value before atmospheric correction. The percentage reduction in bias was calculated from the change in its absolute magnitude before and after correction. Compared with the values before correction, atmospheric correction reduced the root mean square error by approximately 71% to 76% for the two band pairs involving 490 nm and by approximately 27% to 36% for the 670 and 865 nm pair. Across all band pairs for both sensors, the absolute bias decreased by approximately 87% to 94%. For POLDER-3, the biases across the three band pairs ranged from 6.781×10^{-3} to 31.504×10^{-3} before correction and from -3.625×10^{-3} to -0.760×10^{-3} after correction. For DPC-2, the biases ranged from 5.978×10^{-3} to 29.394×10^{-3} before correction to -2.232×10^{-3} to -0.794×10^{-3} after correction. The increase in correlation was most pronounced for the band pairs involving 490 nm. For POLDER-3, the correlation coefficients for the 490 and 670 nm pair and the 490 and 865 nm pair increased from 0.837 and 0.684 before correction to 0.880 and 0.827 after correction, respectively. For DPC-2, the corresponding coefficients increased from 0.846 and 0.687 to 0.912 and 0.827. By contrast, the correlation coefficient for the 670 and 865 nm pair was already approximately 0.92 before correction and remained at a similar level after correction, although its root mean square error and absolute bias decreased further. These results show that, although the corrected band-specific R_p values may still be affected by instrument response, observational error and surface composition, atmospheric correction effectively reduces the differences among bands and brings their spectral variation closer to the expected weak spectral dependence of land-surface polarized reflectance.

https://doi.org/10.5194/essd-2026-834
Preprint. Discussion started: 4 November 2026
© Author(s) 2026. CC BY 4.0 License.

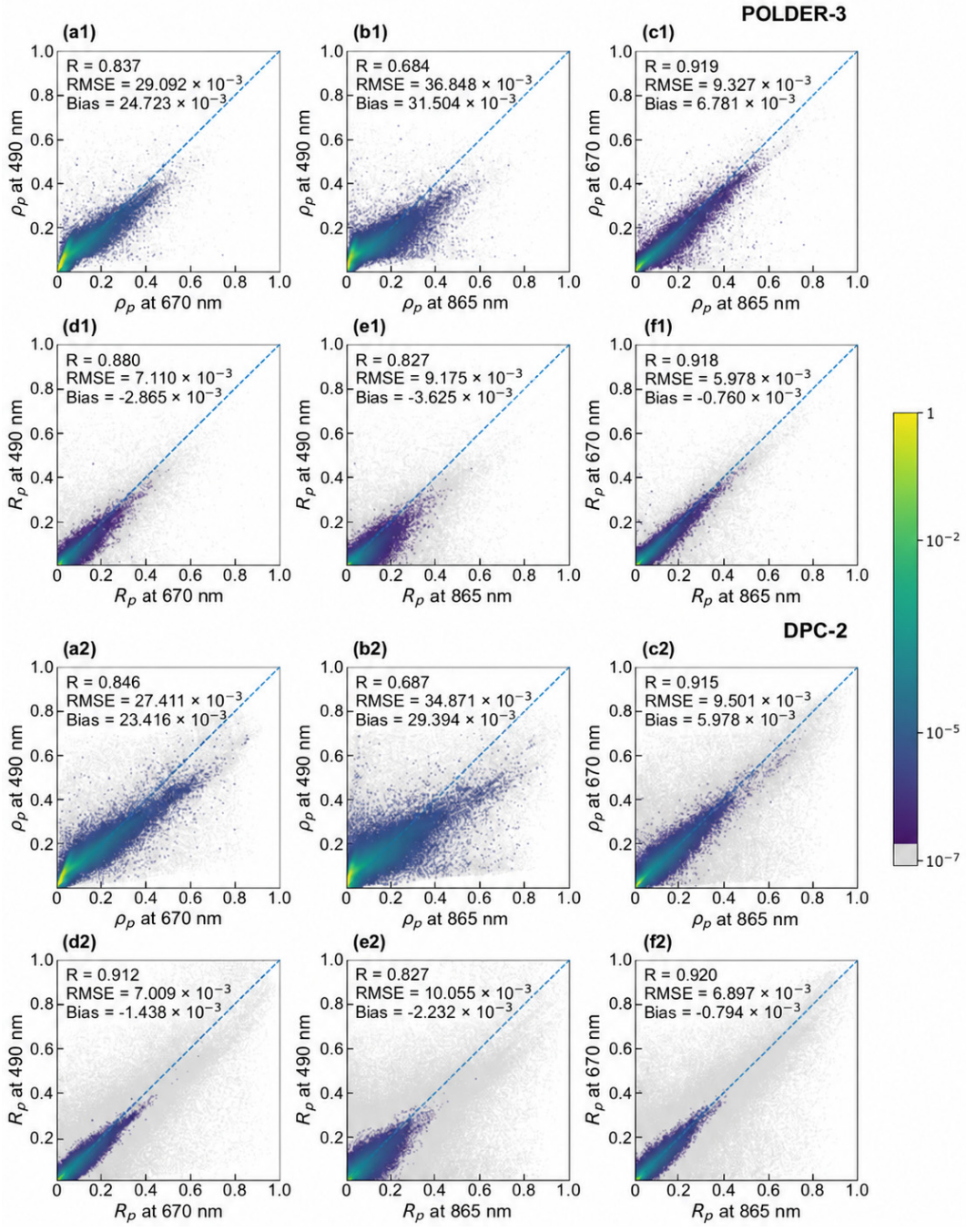


Figure 2. Cross-band comparisons of POLDER-3 and DPC-2 polarized reflectance before and after atmospheric correction. The upper two rows show the POLDER-3 results, and the lower two rows show the DPC-2 results. Panels (a)–(c) show the top of atmosphere ρ_p before atmospheric correction for the two sensors. Panels (d)–(f) show the corresponding band-specific R_p retrieved after correcting for both molecular and aerosol effects. The first column compares 490 and 670 nm, the second compares 490 and 865 nm, and the third compares

https://doi.org/10.5194/essd-2026-834
Preprint. Discussion started: 4 November 2026
© Author(s) 2026. CC BY 4.0 License.



670 and 865 nm. Each point represents one directional observation for which both corresponding bands are valid. Bias is calculated as the value for the wavelength on the vertical axis minus that for the wavelength on the horizontal axis. The blue dashed lines indicate the 1:1 relationship. Point colour indicate the normalized local point density on a logarithmic scale, with light grey corresponding to regions of the lowest point density.

To examine how the cross-band differences varied with aerosol loading and observation geometry, Figure 3 compares their distributions as functions of AOD_{550} and SA before and after correction. Before correction, the cross-band differences in TOA polarized reflectance were predominantly positive, with the largest differences for the 490–865 nm pair and the smallest for the 670–865 nm pair. No clear monotonic dependence on AOD_{550} was observed, whereas the SA dependence was more pronounced: differences involving 490 nm were largest at approximately 70–110° and approached zero as SA increased toward 180°. After atmospheric correction, all three band-pair differences became more closely centered around zero, and their SA dependence weakened substantially. Negative differences and relatively large dispersion nevertheless remained at SA below approximately 60°. Atmospheric correction therefore reduced, but did not completely eliminate, wavelength- and geometry-dependent differences. This improvement provides an internal basis for treating the three corrected bands as estimates of a common R_p in the subsequent weighted fusion, but it does not constitute an independent validation of atmospheric-correction accuracy.

https://doi.org/10.5194/essd-2026-834
Preprint. Discussion started: 4 November 2026
© Author(s) 2026. CC BY 4.0 License.

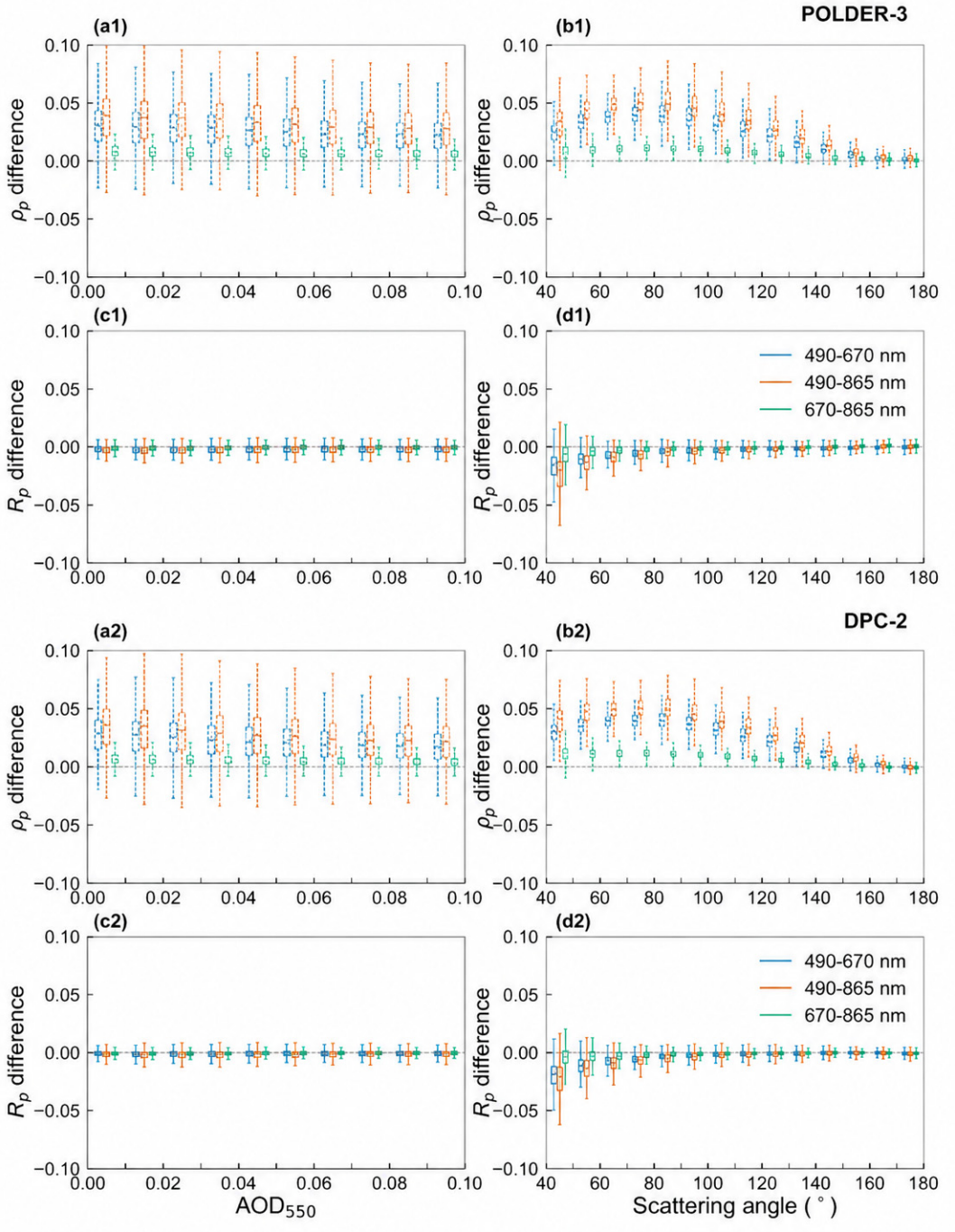


Figure 3. Cross-band differences in POLDER-3 and DPC-2 polarized reflectance before and after atmospheric correction. Panels (a) and (b) show the TOA apparent polarized reflectance before correction as functions of AOD_{550} and scattering angle, respectively. Panels (c) and (d) show the corresponding band-specific R_p differences after correction for molecular and aerosol effects. Cross-band differences are calculated as the value at the shorter wavelength minus that at the longer wavelength.

https://doi.org/10.5194/essd-2026-834
Preprint. Discussion started: 4 November 2026
© Author(s) 2026. CC BY 4.0 License.



5. Database characteristics, quality assessment, and cross-sensor consistency

5.1. Spatial coverage and sample characteristics

To characterize the geographical coverage of valid observations in the two databases, Figure 4 shows the spatial distribution of valid collocations between satellite observations and AERONET measurements on the common geographical grid defined in the Methods. Each circle represents an AERONET site containing valid collocations rather than the locations of all AERONET sites, which accounts for the gridded appearance of the maps. Valid observations cover North and South America, Europe, Africa, Asia and Oceania, but are concentrated primarily in North America and Europe. Coverage is comparatively sparse across much of Africa, central and northern Asia, South America and high latitude regions. Most valid grid cells fall within the lowest category of normalized spatial sampling density, whereas higher values are concentrated in a limited number of regions in North America and Europe. Because the annual sampling fractions were normalized separately for the two sensors, the maps show the relative spatial distribution of sampling within each database rather than absolute differences in the number of AERONET sites or the frequency of valid observations. Thus, although the two databases show broadly similar geographical coverage, this similarity does not imply that the two periods contain the same numbers of AERONET sites or valid observations. Spatial sampling in both databases remains uneven owing to the spatial distribution of AERONET sites.

https://doi.org/10.5194/essd-2026-834
Preprint. Discussion started: 4 November 2026
© Author(s) 2026. CC BY 4.0 License.

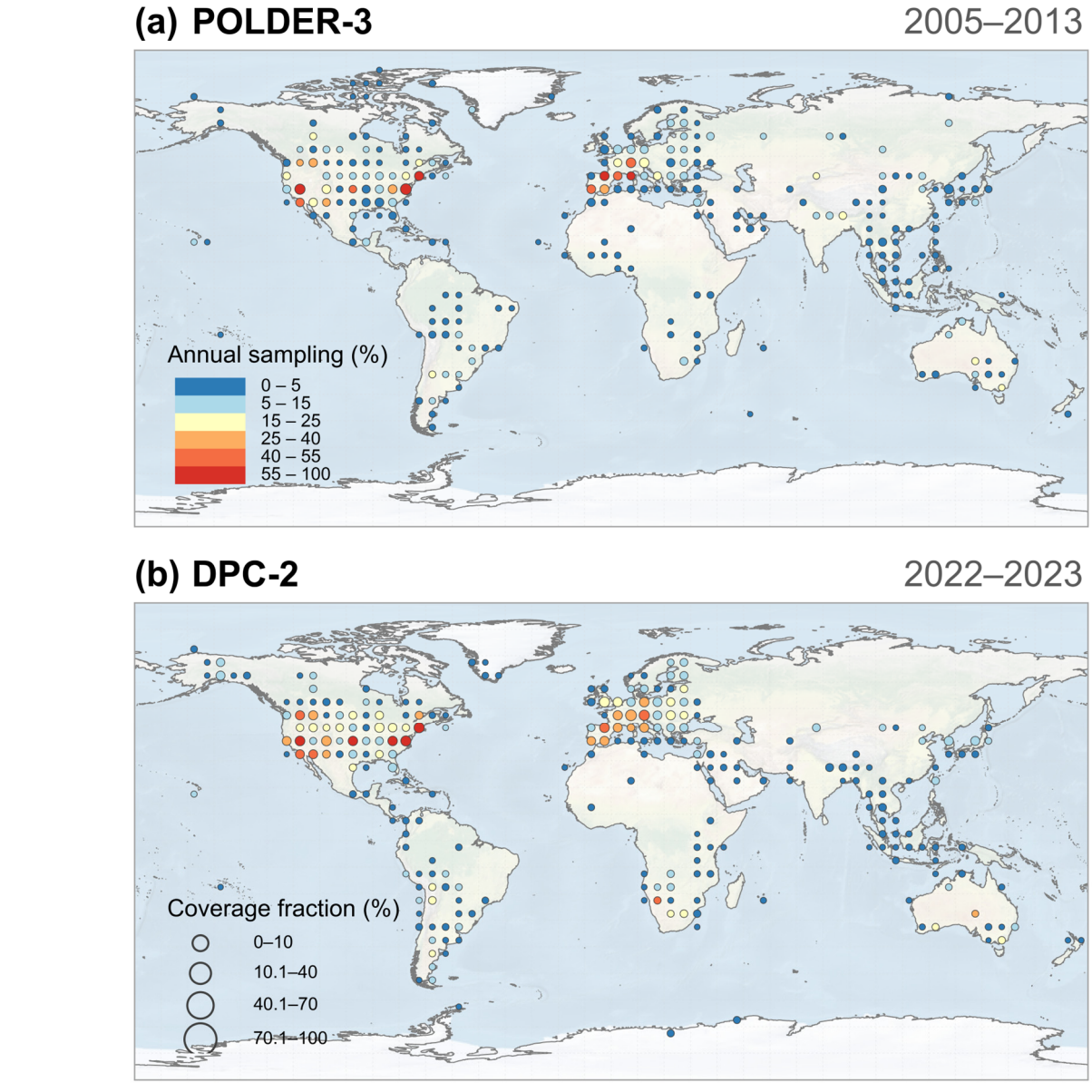
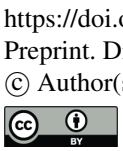


Figure 4. Spatial distribution and sampling characteristics of the observations used to construct the BPDF databases for (a) POLDER-3 during 2005–2013 and (b) DPC-2 during 2022–2023. Circle color indicates the normalized spatial sampling density, and circle size indicates the coverage fraction. The color and symbol-size categories shown in the legends apply to both panels.

To compare sample volume and observation geometry between the two databases and to establish the sampling basis for the subsequent cross-sensor analysis, Figure 5 summarizes the valid directional observations from the two sensors. Although DPC-2 covers a shorter observation period, it contains 5,451,719 valid directional observations, compared with 2,350,808 for

https://doi.org/10.5194/essd-2026-834
Preprint. Discussion started: 4 November 2026
© Author(s) 2026. CC BY 4.0 License.



POLDER-3. Panels (a) and (e) provide a broad overview of the represented surface groups, whereas the detailed class-level land-cover composition is examined separately in Fig. 6. SZAs in both databases occur mainly between approximately 20 and 65°. The POLDER-3 sample fraction reaches its maximum at approximately 55 to 60°, whereas DPC-2 is more uniformly distributed across this range. VZAs extend from near nadir to approximately 65° but are concentrated mainly between 30 and 60°, with the largest sample fractions occurring between 45 and 55°. SAs span approximately 50 to 180° and are concentrated mainly between 80 and 160°. Both databases reach their maximum SA sample fraction at approximately 120°, although DPC-2 contains a slightly larger fraction at high SAs. Overall, the two databases cover a broad common range of observation geometries, although angular sampling within this range is not uniform.

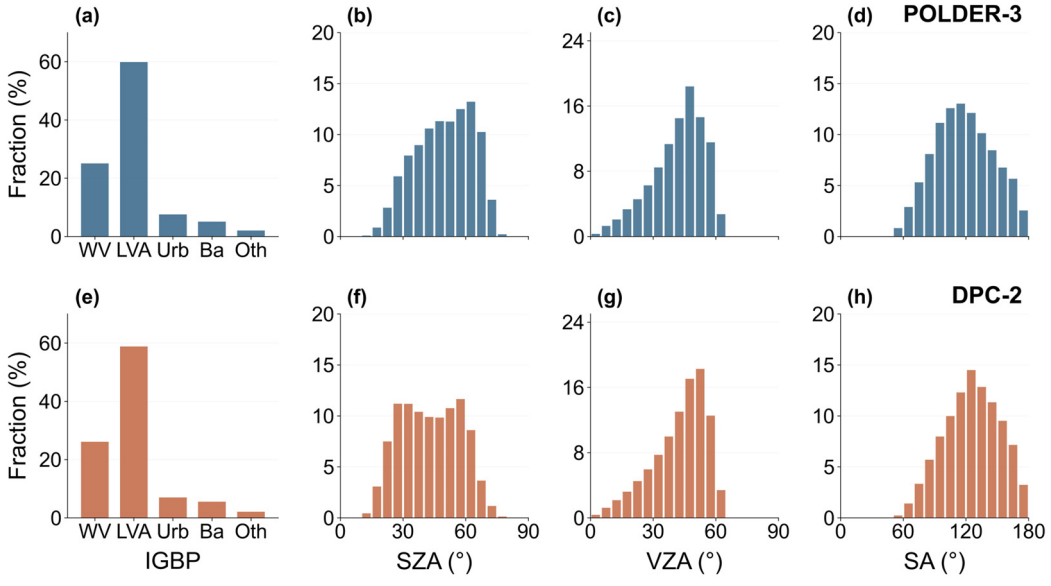


Figure 5. Land-cover composition and observation-geometry distributions of valid directional observations in the POLDER-3 and DPC-2 BPDF databases. Panels (a) and (e) show land-cover composition at the observation-sequence level. Panels (b) and (f), (c) and (g), and (d) and (h) show SZA, VZA and SA distributions at the directional-observation level. The abbreviations are WV for woody vegetation, LVA for low vegetation and agricultural surfaces, UB for urban surfaces, Br for barren surfaces and Oth for other IGBP land-cover types, including permanent wetlands, snow and ice, and water bodies. Panels (b) and (f), (c) and (g), and (d) and (h) show the distributions of SZA, VZA and SA, respectively.

Figure 6 further shows the distribution of valid observation sequences across dominant IGBP land-cover classes in the two databases. Grasslands are the most abundant class, accounting for 20.4% of DPC-2 observation sequences and 20.7% of POLDER-3 observation sequences, followed by croplands at 19.5% and 21.5%, respectively. Woody savannas account for

https://doi.org/10.5194/essd-2026-834
Preprint. Discussion started: 4 November 2026
© Author(s) 2026. CC BY 4.0 License.


10.4% and 10.9%, whereas savannas account for 9.6% and 10.8%. Together, these four classes represent 59.9% of the valid DPC-2 observation sequences and 63.9% of the valid POLDER-3 observation sequences. Urban and barren surfaces account for 7.2% and 5.7% of DPC-2 observation sequences and 7.5% and 5.2% of POLDER-3 observation sequences, respectively. The largest class-specific difference occurs for deciduous broadleaf forest, which accounts for 6.8% of DPC-2 observation sequences and 4.0% of POLDER-3 observation sequences. Closed shrublands, permanent wetlands, and snow and ice each account for no more than 0.2% of either database. Overall, the dominant IGBP land-cover compositions of the two databases are similar, with differences in class proportions not exceeding 2.8%.

https://doi.org/10.5194/essd-2026-834
Preprint. Discussion started: 4 November 2026
© Author(s) 2026. CC BY 4.0 License.

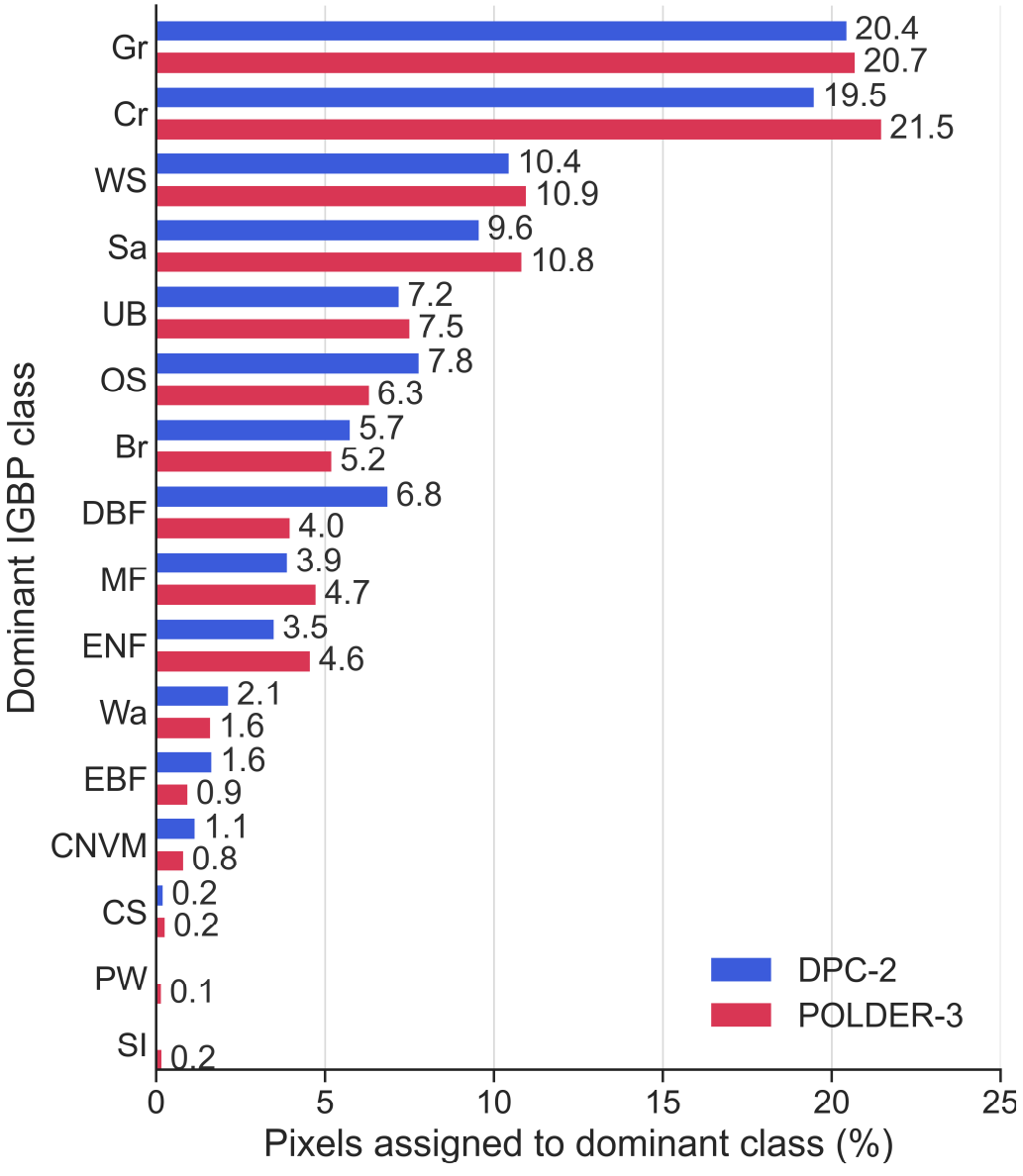


Figure 6. Distribution of valid observation sequences in the POLDER-3 and DPC-2 BPDF databases across dominant IGBP land-cover classes. Blue and red bars represent DPC-2 and POLDER-3, respectively. The displayed classes are evergreen broadleaf forest (EBF), evergreen needleleaf forest (ENF), deciduous broadleaf forest (DBF), mixed forests (MF), urban and built-up lands (UB), closed shrublands (CS), open shrublands (OS), woody savannas (WS), barren land (Br), cropland and natural vegetation mosaics (CNVM), savannas (Sa), grasslands (Gr), permanent wetlands (PW), permanent snow and ice (SI) and croplands (Cr).

https://doi.org/10.5194/essd-2026-834
Preprint. Discussion started: 4 November 2026
© Author(s) 2026. CC BY 4.0 License.

Open Access Earth System Science Data Discussions

5.2. Quality-assurance statistics

To characterize the internal quality assigned to each directional observation, Figure 7a summarizes the overall QA grade distributions of the two databases. QA_3 accounts for 45.3% of the DPC-2 directional observations and 36.4% of the POLDER-3 directional observations, whereas QA_2 or higher accounts for 72.8% and 67.5%, respectively. The proportions of QA_0 are nearly identical in the two databases, but DPC-2 contains a larger proportion of QA_3 observations and correspondingly smaller proportions of QA_1 and QA_2 observations. Figure 7b compares the proportions of each QA component attaining QA_3 and QA_2 or higher. For angular sampling, SZA, VZA and band coverage, more than 97% of the directional observations attain QA_2 or higher. Band coverage attains QA_3 for approximately 91% of the observations in both databases. Surface homogeneity attains QA_3 for 66% of the DPC-2 observations and 56% of the POLDER-3 observations, whereas QA_3 is also less frequent for band fusion. The contrast between band coverage and band fusion indicates that valid bands are generally sufficient, although the QA grades propagated through weighted fusion do not always remain high. Because the quality components are not independent, these proportions describe the frequency of lower grades within each component and cannot be interpreted as independent causes of the overall QA distribution. Figure 7c compares the QA grade composition among IGBP land-cover classes. Barren surfaces contain the largest proportions of high-grade observations in both databases. Open shrublands, croplands, urban surfaces and grasslands also contain relatively large proportions of high-grade observations. The QA_3 proportions for mixed forests, woody savannas, and cropland and natural vegetation mosaics are lower, at approximately 16% to 25%. Permanent wetlands exhibit the largest cross-sensor difference, with QA_2 or higher accounting for 35.0% of the DPC-2 observations and 59.2% of the POLDER-3 observations. Except for permanent wetlands, the QA_3 proportion is higher for DPC-2 across most of the displayed land-cover classes, consistent with the overall distributions in Figure 7a. These class-specific statistics can support QA screening for different surface types but should not be interpreted as an inherent accuracy ranking among land-cover classes. Overall, the QA flags provide a basis for tiered use of the databases. Restricting the data to QA_3 applies more stringent internal quality constraints, whereas retaining observations at QA_2 or higher preserves a larger sample size.

https://doi.org/10.5194/essd-2026-834
Preprint. Discussion started: 4 November 2026
© Author(s) 2026. CC BY 4.0 License.

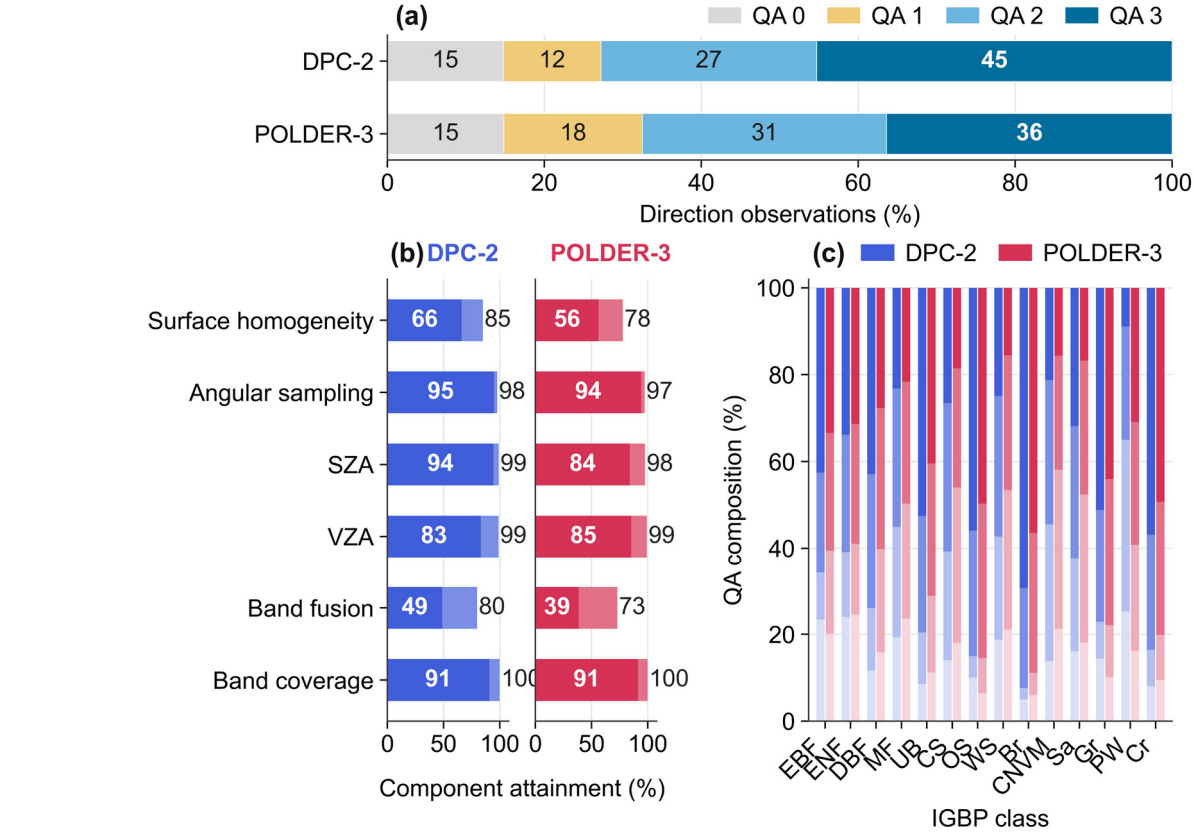
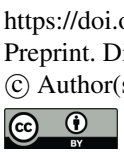


Figure 7. QA summary for the POLDER-3 and DPC-2 BPDF databases. (a) Percentage of directional observations assigned to the four overall quality grades. The values within the stacked bars indicate the percentage in each grade. (b) Attainment rates for the six QA components: surface homogeneity, angular sampling, SZA, VZA, band fusion, and band coverage. The dark portions indicate the percentages assigned QA_3, corresponding to the preferred criteria. The complete bars, including the lighter extensions, indicate the percentages assigned QA_2 or QA_3, corresponding to at least the acceptable criteria. (c) Composition of the four QA grades within each dominant IGBP class. Blue and red bars represent DPC-2 and POLDER-3, respectively, with progressively darker shades corresponding to QA_0–QA_3.

5.3. Angular distributions across surface types

Figure 8 compares the distributions of mean R_p across RAA and VZA for four surface groups within three SZA ranges for POLDER-3 and DPC-2. Overall, higher R_p occurs more frequently at larger RAAs and elevated R_p also occur at larger VZAs across many angular regions, although the magnitude and angular extent of these patterns vary among surface types. At SZA = 0° to 30°, low vegetation and agricultural surfaces exhibit clear azimuthal variation, whereas urban and barren surfaces show stronger angular contrasts, with higher R_p occurring mainly at larger RAAs. As SZA increases, the angular domain

https://doi.org/10.5194/essd-2026-834
Preprint. Discussion started: 4 November 2026
© Author(s) 2026. CC BY 4.0 License.



occupied by higher R_p generally expands, particularly for low vegetation and agricultural surfaces, urban surfaces and barren surfaces. At SZA = 30° to 60° and 60° to 90°, the differences among surface types become more pronounced, with barren surfaces generally exhibiting higher R_p than the other groups. Across the common colour scale, both the magnitude of R_p and the strength of its angular variation increase broadly from woody vegetation to low vegetation and agricultural surfaces, urban surfaces and barren surfaces. Although the principal observation periods of the two databases are separated by nearly a decade, they exhibit similar overall angular structures. This qualitative agreement indicates that R_p in the two databases has a similar overall dependence on illumination and viewing geometry.

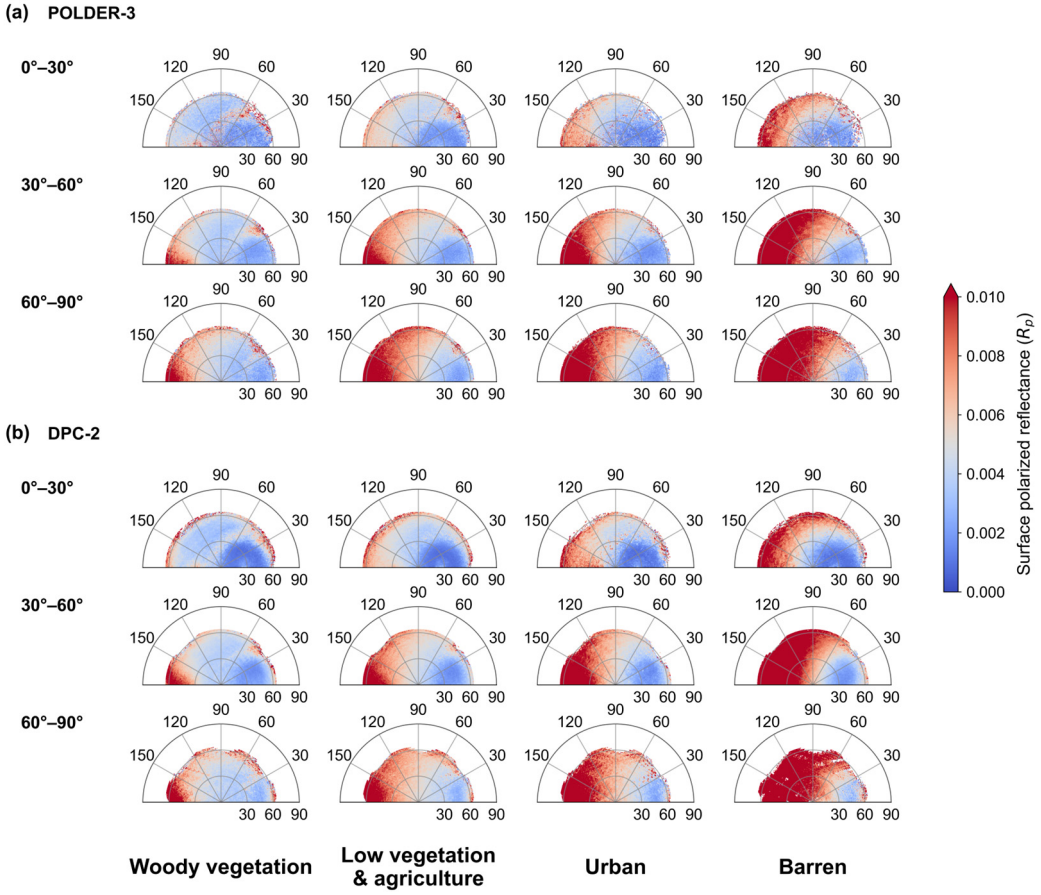


Figure 8. Angular distributions of land-surface polarized reflectance derived from (a) POLDER-3 and (b) DPC-2 observations. The IGBP classes were aggregated into four broader surface groups comprising woody vegetation (WV, including ENF, EBF, DNF, DBF, MF and WS), low vegetation and agriculture (LVA, including CS, OS, Sa, Gr, Cr and CNVM), UB and Br. The rows correspond to SZA intervals of 0 to 30°, 30 to 60° and 60 to 90°. In each polar plot, the angular coordinate represents RAA from 0 to 180°, and the radial coordinate represents VZA from 0 to 90°. Blank regions indicate geometries without valid observations.

https://doi.org/10.5194/essd-2026-834
Preprint. Discussion started: 4 November 2026
© Author(s) 2026. CC BY 4.0 License.

Open Access Earth System Science Data Discussions

5.4. Cross-sensor comparison of surface polarized reflectance

To quantify the statistical correspondence between the two sensor records, Figure 9 compares spatially neighboring POLDER-3 and DPC-2 observations matched by land-cover type and observation geometry. All displayed classes exhibit positive correlations, with R ranging from 0.60 to 0.87. Most matched R_p values are concentrated in the low-value range, while several surface types show greater dispersion at higher R_p. With bias defined as DPC-2 minus POLDER-3, savannas exhibit both the largest positive bias 1.08×10^{-3} and the largest root-mean-square error (RMSE) 7.02×10^{-3}, whereas barren surfaces show the largest negative bias -0.85×10^{-3}. Closed shrublands have the smallest RMSE, at 1.38×10^{-3}. The highest correlations occur for closed shrublands and urban surfaces, followed by cropland–natural vegetation mosaics and barren surfaces. These results show a class-dependent positive correspondence between the two records under the matched spatial, surface and observation-geometry conditions. However, classes close to the minimum display threshold should be interpreted cautiously, and correlation alone does not establish strict agreement or absolute accuracy. Because the observations are not simultaneous and their principal acquisition periods are separated by approximately a decade, the remaining differences may reflect actual surface changes, spatial-resolution differences, residual mismatches in observation conditions, and atmospheric-correction uncertainties.

https://doi.org/10.5194/essd-2026-834
Preprint. Discussion started: 4 November 2026
© Author(s) 2026. CC BY 4.0 License.

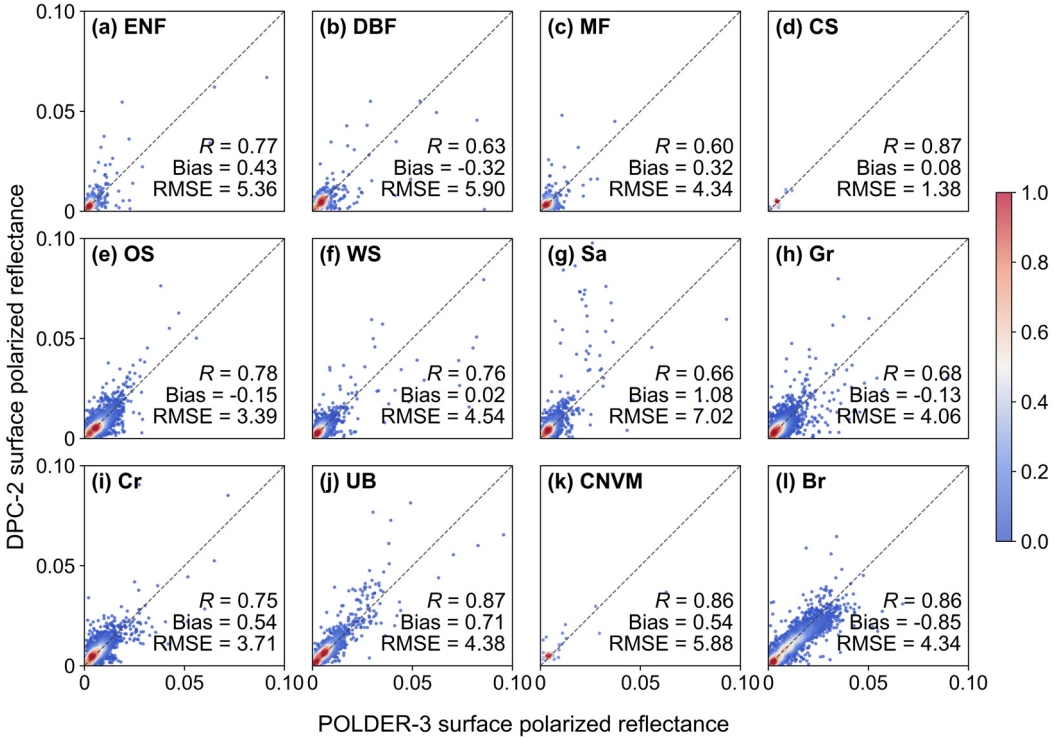
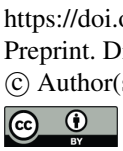


Figure 9. Comparison of land-surface polarized reflectance derived from matched POLDER-3 and DPC-2 observations for different land-cover types indicated in the upper-left corner of each panel. The dashed lines represent the 1:1 relationship, and the colour indicate normalized point density. Only IGBP classes with at least 20 matched pairs are displayed.

5.5. Consistency of semi-empirical BPDF model fitting

To compare the fitting behavior of semi-empirical BPDF models across the two databases, Figure 10 summarizes the RMSEs of six models for different viewing positions and IGBP classes. The two databases produce broadly similar relative model rankings: the Nadal–Bréon and Litvinov models generally yield lower fitting errors, whereas the Diner model generally yields higher errors. RMSE also tends to increase toward both ends of the respective viewing sequences, where larger-VZA observations are sampled. Permanent wetlands exhibit comparatively high RMSE, while the relative ranking of the models varies among the other land-cover classes. The comparatively low RMSEs of the Nadal–Bréon and Litvinov models are consistent with Yang et al. (2017), who identified the same two models as having the lowest mean RMSEs when fitted to POLDER-3 polarized reflectance at 865 nm. More importantly for the present study, the broadly similar relative model rankings and viewing-position dependence obtained from DPC-2 and POLDER-3 indicate that the two databases provide

https://doi.org/10.5194/essd-2026-834
Preprint. Discussion started: 4 November 2026
© Author(s) 2026. CC BY 4.0 License.



530 consistent angular information for fitting semi-empirical BPDF models. This comparison does not imply identical absolute fitting accuracy, isolate the effects of individual sensor characteristics or establish transferability to other spaceborne polarimeters.

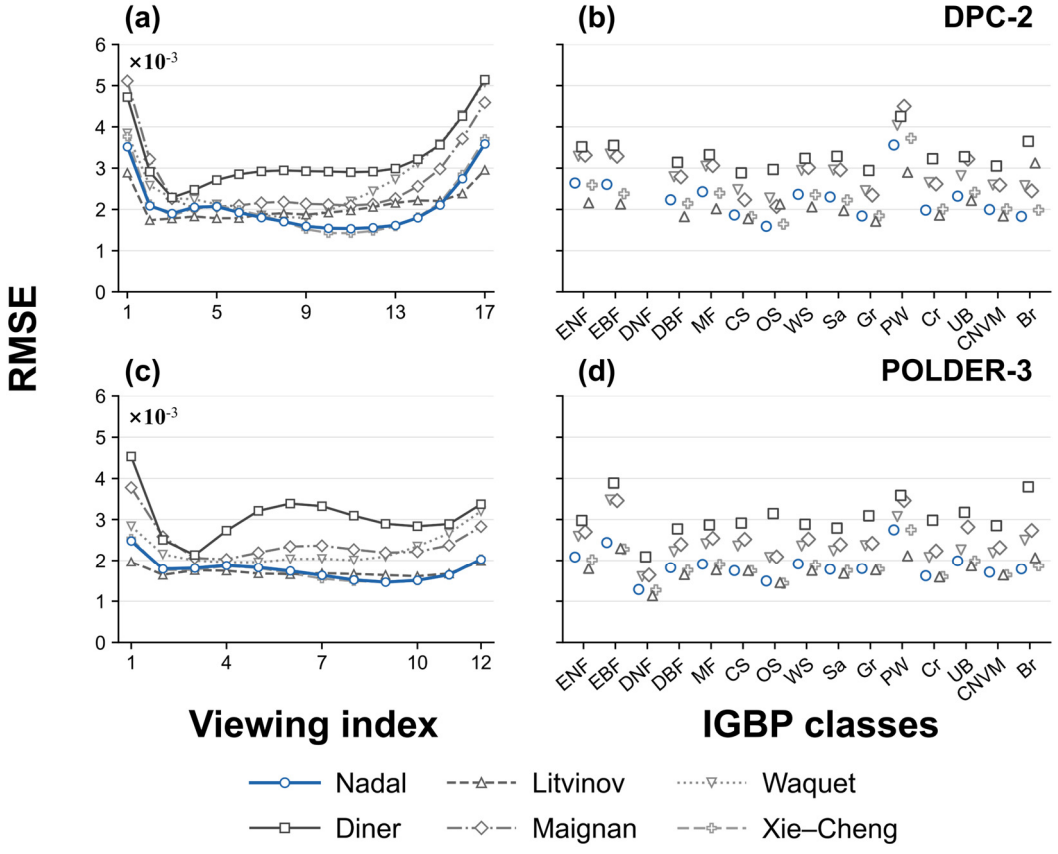


Figure 10. RMSEs of six semi-empirical BPDF models fitted to the DPC-2 and POLDER-3 databases. Panel (a) shows RMSE across the 17
535 DPC-2 viewing indices, and panel (b) shows RMSE across the dominant IGBP land-cover classes for DPC-2. Panel (c) shows RMSE across the 12 POLDER-3 viewing indices, and panel (d) shows RMSE across the dominant IGBP land-cover classes for POLDER-3.

6. Spatial-resolution-associated subpixel mixing and polarized reflectance

Pixels assigned to the same dominant IGBP land-cover class do not necessarily have the same subpixel composition. POLDER-3 has a coarser spatial resolution than DPC-2, and its pixels therefore cover larger areas that may contain more land-cover
540 classes. We therefore compared subpixel land-cover heterogeneity between the two databases and examined the association between MI and R_p at the two spatial resolutions.

https://doi.org/10.5194/essd-2026-834
Preprint. Discussion started: 4 November 2026
© Author(s) 2026. CC BY 4.0 License.



The cumulative probability curve of MI for DPC-2 was generally above that for POLDER-3 (Figure 11a). The mean dominant land-cover fraction was approximately 5.8 percentage points higher for DPC-2 than for POLDER-3, indicating that DPC-2 observation sequences were generally more homogeneous at their native spatial scale. Comparisons within individual IGBP classes further showed that this difference was not solely attributable to differences in the overall land-cover composition of the two databases (Figure 11b). The difference in mean MI between the two databases was defined as $\Delta MI = MI_{DPC-2} - MI_{POLDER-3}$. After correction for multiple comparisons, ΔMI was significantly below zero for EBF, DBF, OS, WS, Sa, Gr, UB, SI and Br. The largest difference occurred for SI, with $\Delta MI = -0.212$, followed by EBF and Sa, with values of −0.110 and −0.106, respectively. PW showed the opposite relationship, with $\Delta MI = 0.113$, whereas the differences for the remaining classes were not significant. Overall, the coarser POLDER-3 observation sequences contained higher proportions of nondominant surface components for most land-cover classes, although the magnitude and direction of this difference varied among classes.

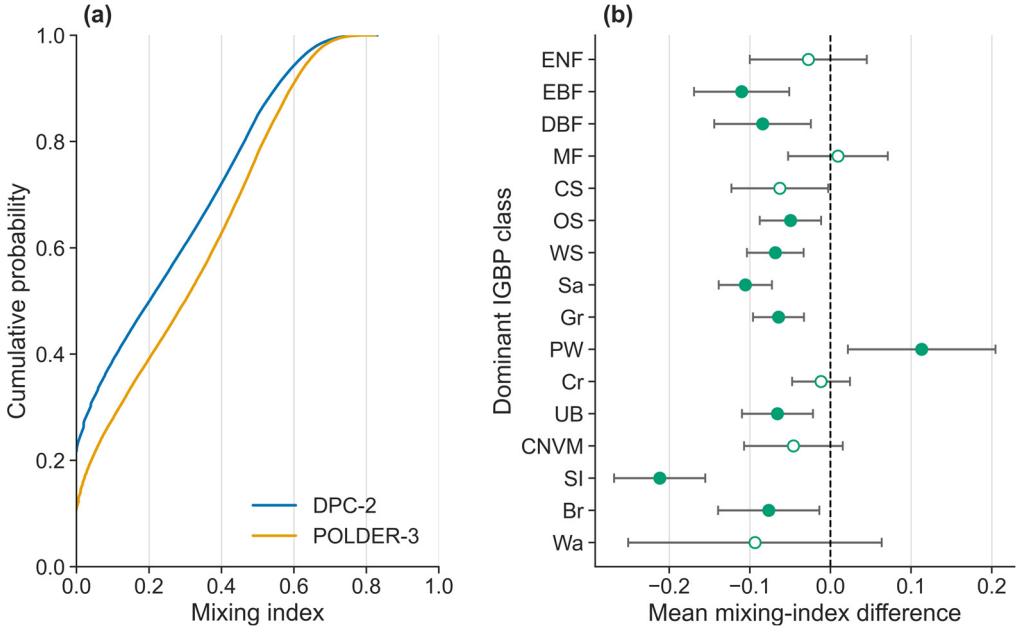


Figure 11. Comparison of subpixel land-cover mixing in the POLDER-3 and DPC-2 BPDF databases. (a) Cumulative probability distributions of the mixing index for DPC-2 (blue) and POLDER-3 (orange). (b) Differences between the class-specific mean mixing indices of DPC-2 and POLDER-3, defined as $\Delta MI = MI_{DPC-2} - MI_{POLDER-3}$. Horizontal bars represent 95% confidence intervals, and the dashed line marks zero difference. Filled and open circles indicate Benjamini–Hochberg-adjusted $q<0.05$ and $q\geq0.05$, respectively. Negative values

https://doi.org/10.5194/essd-2026-834
Preprint. Discussion started: 4 November 2026
© Author(s) 2026. CC BY 4.0 License.



indicate greater mixing in POLDER-3. Class-specific P values were adjusted using the Benjamini and Hochberg procedure to control the false-discovery rate within each sensor.

The pixel median R_p gradually decreased with increasing MI in both databases before approaching a relatively stable level (Figure 12a). After adjustment for observation geometry, a 0.1 increase in MI was associated with a mean decrease in R_p of 0.43×10^{-4} for POLDER-3 and 0.04×10^{-4} for DPC-2. This result indicates that the association between R_p and subpixel composition was stronger for POLDER-3 than for DPC-2. This overall relationship masked clear differences among land-cover classes (Figure 12b). ENF, DBF, MF and WS showed significant positive associations in both databases, whereas UB and Br showed significant negative associations in both. Gr and Cr showed significant negative associations only for POLDER-3, whereas Wa showed a significant negative association only for DPC-2. Among the six classes with significant associations for both sensors, the absolute point estimates of the POLDER-3 regression coefficients were approximately 1.3 to 2.1 times those for DPC-2. This result further indicates that the class dependent relationships between MI and R_p were stronger for POLDER-3. The presence of both positive and negative associations among IGBP classes shows that subpixel mixing does not shift R_p towards a common value across all surface types. MI represents only the total fractional area of nondominant surface components, whereas the direction of the change in R_p also depends on the difference in polarized reflectance between the dominant surface and the nondominant components. Positive coefficients are consistent with nondominant components having a higher mean R_p than the dominant surface, whereas negative coefficients are consistent with the opposite contrast. Because MI does not identify the specific nondominant land-cover classes, it cannot by itself separate the contributions of individual surface components.

https://doi.org/10.5194/essd-2026-834
Preprint. Discussion started: 4 November 2026
© Author(s) 2026. CC BY 4.0 License.

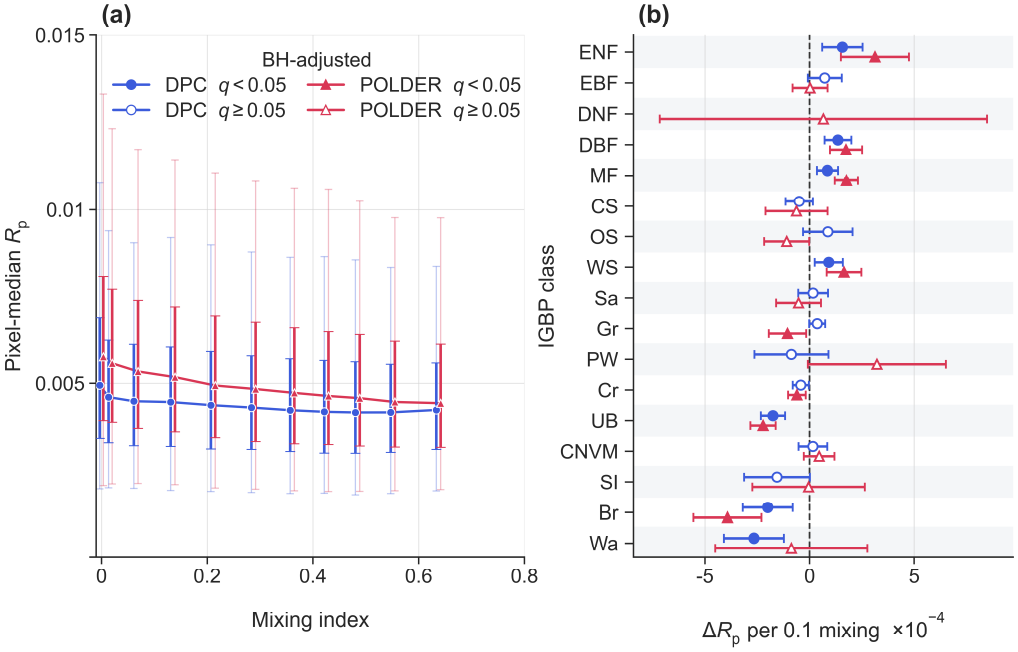


Figure 12. Association between land-surface polarized reflectance and subpixel land-cover mixing. (a) Pixel-median R_p summarized within common quantile-spaced mixing-index bins. Blue circles and red triangles represent DPC-2 and POLDER-3, respectively. Thick and thin vertical intervals show the interquartile and 5th–95th percentile ranges. (b) Change in R_p associated with a 0.1-unit increase in MI after adjustment for the standardized linear and quadratic terms of SZA, VZA, and RAA, estimated separately for each sensor and dominant IGBP class. Estimates are expressed in units of 10^{-4}. Horizontal bars represent 95% confidence intervals, and the dashed line marks zero change. Filled and open symbols indicate q<0.05 and q≥0.05, respectively, after Benjamini and Hochberg correction within each sensor. DNF denotes deciduous needleleaf forest, and Wa denotes water bodies.

7. Conclusion

This study presents two BPDF databases derived from POLDER-3 and DPC-2 using a common framework for aerosol correction, multiband fusion, data organization and quality assurance. By combining AERONET AOD with 6SV vector radiative transfer calculations and applying the same processing principles to both sensors, the framework extends BPDF database construction beyond previous single-band and single-sensor approaches. The resulting databases provide fused R_p with consistent variable definitions and observation-level QA information while retaining the native angular sampling and spatial resolution of each sensor. The results show that aerosol effects cannot be neglected even under low aerosol loading. After consistent atmospheric correction, the multiband results exhibit greater spectral consistency. The two databases also

https://doi.org/10.5194/essd-2026-834
Preprint. Discussion started: 4 November 2026
© Author(s) 2026. CC BY 4.0 License.



show clear correspondence under similar land-cover and observation-geometry conditions, together with consistent overall angular structures and semi-empirical model fitting performance. Taken together, these findings support the applicability of the common processing framework to POLDER-3 and DPC-2 under the sampling and atmospheric conditions examined here. The two databases therefore provide a consistent basis for linking historical POLDER-3 observations with more recent DPC-2 observations. The analysis of subpixel land-cover heterogeneity further reveals the influence of spatial scale on surface polarization. The association between R_p and subpixel composition is stronger at the coarser POLDER-3 resolution, and this relationship varies among land-cover classes. Cross-sensor BPDF comparisons and the construction of surface polarization priors must therefore account not only for atmospheric correction and observation geometry, but also for spatial resolution, pixel homogeneity and polarization differences among surface components. Incorporating spatial-scale effects into BPDF database assessment provides a basis for interpreting apparent sensor differences in relation to subpixel surface composition and provides a basis for the coordinated use of observations at different spatial resolutions. The current databases remain limited in spatial coverage and sample representativeness. The POLDER-3 and DPC-2 records do not overlap in time, and no independent global reference for surface R_p is available. The cross-sensor comparison therefore quantifies conditional correspondence under matched surface and observation conditions rather than absolute retrieval accuracy or point-by-point equivalence between the two databases. Valid observations depend on collocations with AERONET sites and are restricted to low-aerosol-loading conditions, and therefore do not provide uniform sampling of the global land surface. The difficulty of obtaining robust and complete aerosol microphysical properties under low aerosol loading also requires the use of a prescribed prescribed continental aerosol model for atmospheric correction. Sensitivity analysis indicates that this assumption produces relatively small differences under most observation geometries, although caution is required at large solar zenith angles and under oblique viewing conditions. The applicability of the databases and their quality flags should therefore be considered together with their sampling conditions and atmospheric correction assumptions. The two databases provide surface polarization observations with consistent variable definitions, explicit QA information and comparable processing workflows. They can support the development and evaluation of semi-empirical and data-driven BPDF models and facilitate analyses of surface polarization across land-cover types, observation geometries and spatial scales. Future multisensor BPDF records should retain the fractional area of each land-cover class or an equivalent pixel-mixing metric in addition to the dominant class.

https://doi.org/10.5194/essd-2026-834
Preprint. Discussion started: 4 November 2026
© Author(s) 2026. CC BY 4.0 License.


This information would facilitate interpretation of resolution-dependent differences in surface polarized reflectance and improve the reuse of the databases across-sensors with different spatial resolutions As surface boundary conditions for vector radiative transfer calculations, the databases can also provide better-characterized and internally consistent surface polarization priors for polarimetric aerosol retrievals, helping to reduce retrieval errors associated with inadequate representation of the surface polarization signal and supporting greater consistency among retrievals from different polarimetric sensors. By connecting historical POLDER-3 observations with the newer generation of DPC-2 observations, this work also provides a basis for constructing long-term multisensor records of land-surface polarized reflectance and provides a basis for advancing BPDF model development, studies of surface polarization, and polarimetric retrievals of aerosols and other atmospheric properties.

Data availability

The developed land surface polarized reflectance dataset is accessible through Science Data Bank at https://www.scidb.cn/anonymous/bXV1RXJx (doi: 10.57760/sciencedb.015ek) (Ji and Li, 2026). The POLDER-3/PARASOL data were available through ICARE at http://icare.univ-lille1.fr. The DPC/GF-5(02) data were available through CRESDA at https://data.cresda.cn/.

Author contributions

Z.J. conceived the study, developed the methodology and model, performed the analysis, and wrote the original manuscript. Z.L. supervised the study and provided funding support. G.d.L., C.C., Y.C., Z.Z., and L.Z. reviewed and revised the manuscript and provided constructive comments and suggestions.

Competing interests

The authors declare that they have no conflict of interest. Acknowledgements

https://doi.org/10.5194/essd-2026-834
Preprint. Discussion started: 4 November 2026
© Author(s) 2026. CC BY 4.0 License.

Acknowledgement

We thank the AERONET principal investigators and site managers for maintaining the observation sites and providing the measurements used in this study. We also acknowledge the China Centre for Resources Satellite Data and Application (CRESDA) for providing the DPC-2/GF-5(02) data, the CNES and AERIS/ICARE Data and Services Center for providing the POLDER-3/PARASOL data, and the NASA Land Processes Distributed Active Archive Center (LAADS DAAC) for providing the MODIS products. This work was supported by the Jing-Jin-Ji Regional Integrated Environmental Improvement–National Science and Technology Major Project of the Ministry of Ecology and Environment of China, Grant No. 2025ZD1200900 and the Chinese Academy of Sciences President's International Fellowship Initiative, Grant No. 2025PVA0014_Y1.

References

Benjamini, Y. and Hochberg, Y.: Controlling the False Discovery Rate: A Practical and Powerful Approach to Multiple Testing, Journal of the Royal Statistical Society: Series B (Methodological), 57, 289–300, https://doi.org/https://doi.org/10.1111/j.2517-6161.1995.tb02031.x, 1995.

Bréon, F.-M. and Maignan, F.: A BRDF–BPDF database for the analysis of Earth target reflectances, Earth System Science Data, 9, 31–45, https://doi.org/10.5194/essd-9-31-2017, 2017.

Bréon, F.-M., Tanre, D., Lecomte, P., and Herman, M.: Polarized reflectance of bare soils and vegetation: measurements and models, IEEE Transactions on Geoscience and Remote Sensing, 33, 487–499, https://doi.org/10.1109/TGRS.1995.8746030, 1995.

Cameron, A. C. and Miller, D. L.: A Practitioner's Guide to Cluster-Robust Inference, J Hum Resour, 50, 317, https://doi.org/10.3368/jhr.50.2.317, 2015.

Cameron, A. C., Gelbach, J. B., and Miller, D. L.: Robust Inference With Multiway Clustering, Journal of Business & Economic Statistics, 29, 238–249, https://doi.org/10.1198/jbes.2010.07136, 2011.

Dahlback, A. and Stamnes, K.: A new spherical model for computing the radiation field available for photolysis and heating at twilight, Planetary and Space Science, 39, 671–683, https://doi.org/https://doi.org/10.1016/0032-0633(91)90061-E, 1991.

Diner, D. J., Xu, F., Martonchik, J. V., Rheingans, B. E., Geier, S., Jovanovic, V. M., Davis, A., Chipman, R. A., and McClain, S. C.: Exploration of a Polarized Surface Bidirectional Reflectance Model Using the Ground-Based Multiangle SpectroPolarimetric Imager, Atmosphere, 3, 591–619, https://doi.org/10.3390/atmos3040591, 2012.

https://doi.org/10.5194/essd-2026-834
Preprint. Discussion started: 4 November 2026
© Author(s) 2026. CC BY 4.0 License.



Franch, B., Vermote, E. F., Sobrino, J. A., and Fédèle, E.: Analysis of directional effects on atmospheric correction, Remote Sensing of Environment, 128, 276–288, https://doi.org/https://doi.org/10.1016/j.rse.2012.10.018, 2013.

Franks, S., Neigh, C. S. R., Campbell, P. K., Sun, G., Yao, T., Zhang, Q., Huemmrich, K. F., Middleton, E. M., Ungar, S. G., and Frye, S. W.: EO-1 Data Quality and Sensor Stability with Changing Orbital Precession at the End of a 16 Year Mission, Remote Sensing, 9, https://doi.org/10.3390/rs9050412, 2017.

Giles, D. M., Sinyuk, A., Sorokin, M. G., Schafer, J. S., Smirnov, A., Slutsker, I., Eck, T. F., Holben, B. N., Lewis, J. R., Campbell, J. R., Welton, E. J., Korkin, S. V., and Lyapustin, A. I.: Advancements in the Aerosol Robotic Network (AERONET) Version 3 database – automated near-real-time quality control algorithm with improved cloud screening for Sun photometer aerosol optical depth (AOD) measurements, Atmospheric Measurement Techniques, 12, 169–209, https://doi.org/10.5194/amt-12-169-2019, 2019.

Hasekamp, O. P. and Landgraf, J.: Retrieval of aerosol properties over land surfaces: capabilities of multiple-viewing-angle intensity and polarization measurements, Appl. Opt., 46, 3332–3344, https://doi.org/10.1364/AO.46.003332, 2007.

He, Y., Yang, B., Lin, H., and Zhang, J.: Modeling Polarized Reflectance of Natural Land Surfaces Using Generalized Regression Neural Networks, Remote Sensing, 12, https://doi.org/10.3390/rs12020248, 2020.

Holben, B. N., Eck, T. F., Slutsker, I., Tanré, D., Buis, J. P., Setzer, A., Vermote, E., Reagan, J. A., Kaufman, Y. J., Nakajima, T., Lavenu, F., Jankowiak, I., and Smirnov, A.: AERONET—A Federated Instrument Network and Data Archive for Aerosol Characterization, Remote Sensing of Environment, 66, 1–16, https://doi.org/https://doi.org/10.1016/S0034-4257(98)00031-5, 1998.

Jethva, H., Torres, O., Waquet, F., Chand, D., and Hu, Y.: How do A-train sensors intercompare in the retrieval of above-cloud aerosol optical depth? A case study-based assessment, Geophysical Research Letters, 41, 186–192, https://doi.org/https://doi.org/10.1002/2013GL058405, 2014.

Ji, Z. and Li, Z.: A Multi-Angle Land Surface Polarized Reflectance Dataset from DPC-2 and POLDER-3[DS/OL]. V1. Science Data Bank, 2026[2026-10-13], https://doi.org/10.57760/sciencedb.015ek, 2026.

Ji, Z., Li, Z., Zhang, Z., Fu, G., Hasekamp, O., Fan, C., Liu, Q., and de Leeuw, G.: Retrieval of Aerosol Properties Over the Ocean Using Data From the Second-Generation Directional Polarization Camera (DPC-2) Onboard the GF-5(02) Satellite, Journal of Geophysical Research: Atmospheres, 130, e2025JD043908, https://doi.org/https://doi.org/10.1029/2025JD043908, 2025.

Kotchenova, S. Y., Vermote, E. F., Matarrese, R., and Klemm, Jr., F. J.: Validation of a vector version of the 6S radiative transfer code for atmospheric correction of satellite data. Part I: Path radiance, Applied Optics, 45, 6762–6774, https://doi.org/10.1364/AO.45.006762, 2006.

https://doi.org/10.5194/essd-2026-834
Preprint. Discussion started: 4 November 2026
© Author(s) 2026. CC BY 4.0 License.



Lallart, P., Kahn, R., and Tanré, D.: POLDER2/ADEOSII, MISR, and MODIS/Terra reflectance comparisons, Journal of Geophysical Research: Atmospheres, 113, https://doi.org/https://doi.org/10.1029/2007JD009656, 2008.

Litvinov, P., Hasekamp, O., and Cairns, B.: Models for surface reflection of radiance and polarized radiance: Comparison with airborne multi-angle photopolarimetric measurements and implications for modeling top-of-atmosphere measurements, Remote Sensing of Environment, 115, 781–792, https://doi.org/https://doi.org/10.1016/j.rse.2010.11.005, 2011.

Liu, Q., Li, Z., Zhang, Z., Fu, G., Hasekamp, O., Li, L., Bai, Y., and Fan, C.: Polarized reflectance in China from DPC-2/GF-5(02) polarimetric satellite measurements: dataset and model inter-comparison, Journal of Quantitative Spectroscopy and Radiative Transfer, 360, 109961, https://doi.org/https://doi.org/10.1016/j.jqsrt.2026.109961, 2026.

Liu, S., Lin, Y., Yan, L., and Yang, B.: Modeling Bidirectional Polarization Distribution Function of Land Surfaces Using Machine Learning Techniques, Remote Sensing, 12, https://doi.org/10.3390/rs12233891, 2020.

Maignan, F., Bréon, F.-M., Fédèle, E., and Bouvier, M.: Polarized reflectances of natural surfaces: Spaceborne measurements and analytical modeling, Remote Sensing of Environment, 113, 2642–2650, https://doi.org/https://doi.org/10.1016/j.rse.2009.07.022, 2009.

Nadal, F. and Breon, F.-M.: Parameterization of surface polarized reflectance derived from POLDER spaceborne measurements, IEEE Transactions on Geoscience and Remote Sensing, 37, 1709–1718, https://doi.org/10.1109/36.763292, 1999.

Omar, A. H., Won, J.-G., Winker, D. M., Yoon, S.-C., Dubovik, O., and McCormick, M. P.: Development of global aerosol models using cluster analysis of Aerosol Robotic Network (AERONET) measurements, Journal of Geophysical Research: Atmospheres, 110, https://doi.org/https://doi.org/10.1029/2004JD004874, 2005.

Sinyuk, A., Holben, B. N., Eck, T. F., Giles, D. M., Slutsker, I., Korkin, S., Schafer, J. S., Smirnov, A., Sorokin, M., and Lyapustin, A.: The AERONET Version 3 aerosol retrieval algorithm, associated uncertainties and comparisons to Version 2, Atmospheric Measurement Techniques, 13, 3375–3411, https://doi.org/10.5194/amt-13-3375-2020, 2020.

Sulla-Menashe, D., Gray, J. M., Abercrombie, S. P., and Friedl, M. A.: Hierarchical mapping of annual global land cover 2001 to present: The MODIS Collection 6 Land Cover product, Remote Sensing of Environment, 222, 183–194, https://doi.org/https://doi.org/10.1016/j.rse.2018.12.013, 2019.

Tanré, D., Bréon, F. M., Deuzé, J. L., Dubovik, O., Ducos, F., François, P., Goloub, P., Herman, M., Lifermann, A., and Waquet, F.: Remote sensing of aerosols by using polarized, directional and spectral measurements within the A-Train: the PARASOL mission, Atmospheric Measurement Techniques, 4, 1383–1395, https://doi.org/10.5194/amt-4-1383-2011, 2011.

https://doi.org/10.5194/essd-2026-834
Preprint. Discussion started: 4 November 2026
© Author(s) 2026. CC BY 4.0 License.



Vermote, E. F., El Saleous, N., Justice, C. O., Kaufman, Y. J., Privette, J. L., Remer, L., Roger, J. C., and Tanré, D.: Atmospheric correction of visible to middle-infrared EOS-MODIS data over land surfaces: Background, operational algorithm and validation, Journal of Geophysical Research: Atmospheres, 102, 17131–17141, https://doi.org/https://doi.org/10.1029/97JD00201, 1997.

Waquet, F., Goloub, P., Deuzé, J.-L., Léon, J.-F., Auriol, F., Verwaerde, C., Balois, J.-Y., and François, P.: Aerosol retrieval over land using a multiband polarimeter and comparison with path radiance method, Journal of Geophysical Research: Atmospheres, 112, https://doi.org/https://doi.org/10.1029/2006JD008029, 2007.

Waquet, F., Léon, J.-F., Cairns, B., Goloub, P., Deuzé, J.-L., and Auriol, F.: Analysis of the spectral and angular response of the vegetated surface polarization for the purpose of aerosol remote sensing over land, Appl. Opt., 48, 1228–1236, https://doi.org/10.1364/AO.48.001228, 2009.

Xie, D., Cheng, T., Wu, Y., Fu, H., Zhong, R., and Yu, J.: Polarized reflectances of urban areas: Analysis and models, Remote Sensing of Environment, 193, 29–37, https://doi.org/https://doi.org/10.1016/j.rse.2017.02.026, 2017.

Yang, B., Zhao, H., and Chen, W.: Semi-empirical models for polarized reflectance of land surfaces: Intercomparison using space-borne POLDER measurements, Journal of Quantitative Spectroscopy and Radiative Transfer, 202, 13–20, https://doi.org/https://doi.org/10.1016/j.jqsrt.2017.07.014, 2017.

Zhang, Z., Li, Z., Fu, G., Hasekamp, O., Fan, C., Qie, L., Xie, Y., Li, L., Ji, Z., and Liu, Q.: Global Aerosol Retrieval Over Land Using the Chinese Satellite Polarimeter DPC-2/GF-5(02), IEEE Trans. Geosci. Remote Sensing, 63, 1–14, https://doi.org/10.1109/TGRS.2025.3633391, 2025.